



2009

A HEL testbed for high accuracy beam pointing and control

Kim, Dojong

Monterey, California. Naval Postgraduate School

<http://hdl.handle.net/10945/800>



Calhoun is a project of the Dudley Knox Library at NPS, furthering the precepts and goals of open government and government transparency. All information contained herein has been approved for release by the NPS Public Affairs Officer.

Dudley Knox Library / Naval Postgraduate School
411 Dyer Road / 1 University Circle
Monterey, California USA 93943

<http://www.nps.edu/library>



NAVAL POSTGRADUATE SCHOOL

MONTEREY, CALIFORNIA

A HEL Testbed for High Accuracy Beam Pointing
and Control

by

Dojong Kim, Duane Frist, Jae Jun Kim, Brij Agrawal

01 July 2009

Approved for public release; distribution is unlimited

THIS PAGE INTENTIONALLY LEFT BLANK

**NAVAL POSTGRADUATE SCHOOL
Monterey, California 93943-5000**

VADM Daniel Oliver, USN (Ret.)
President

Leonard A. Ferrari
Provost

Reproduction of all or part of this report is authorized.

This report was prepared by:

Dojong Kim
Visiting Scholar of MAE Department
Agency for Defense Development, RoK

Duane Frist
LCDR, USN
MAE Department

Jae Jun Kim
Research Assistant Professor,
MAE Department

Brij Agrawal
Distinguished Professor
MAE Department

Reviewed by:

Released by:

Knox Millsaps
Chair, MAE Department

Karl A. Van Bibber
Vice President and
Dean of Research

THIS PAGE INTENTIONALLY LEFT BLANK

REPORT DOCUMENTATION PAGE			Form Approved OMB No. 0704-0188	
Public reporting burden for this collection of information is estimated to average 1 hour per response, including the time for reviewing instruction, searching existing data sources, gathering and maintaining the data needed, and completing and reviewing the collection of information. Send comments regarding this burden estimate or any other aspect of this collection of information, including suggestions for reducing this burden, to Washington headquarters Services, Directorate for Information Operations and Reports, 1215 Jefferson Davis Highway, Suite 1204, Arlington, VA 22202-4302, and to the Office of Management and Budget, Paperwork Reduction Project (0704-0188) Washington DC 20503.				
1. AGENCY USE ONLY (Leave blank)	2. REPORT DATE July 2009	3. REPORT TYPE AND DATES COVERED Technical Report		
4. TITLE AND SUBTITLE: Title (Mix case letters) A HEL Testbed for High Accuracy Beam Pointing and Control			5. FUNDING NUMBERS	
6. AUTHOR(S) Dojong Kim, Duane Frist, Jae Jun. Kim, Brij Agrawal				
7. PERFORMING ORGANIZATION NAME(S) AND ADDRESS(ES) Naval Postgraduate School Monterey, CA 93943-5000			8. PERFORMING ORGANIZATION REPORT NUMBER	
9. SPONSORING /MONITORING AGENCY NAME(S) AND ADDRESS(ES) N/A			10. SPONSORING/MONITORING AGENCY REPORT NUMBER	
11. SUPPLEMENTARY NOTES The views expressed in this report are those of the author and do not reflect the official policy or position of the Department of Defense or the U.S. Government.				
12a. DISTRIBUTION / AVAILABILITY STATEMENT Approved for public release; distribution is unlimited			12b. DISTRIBUTION CODE A	
13. ABSTRACT (maximum 200 words)				
<p>High energy laser (HEL) weapons are some of most challenging military applications in the future battle fields since the speed of light delivery enables the war fighter to engage very distant targets immediately. The issues of the technology on the HEL system include various types of high energy laser devices, beam control systems, atmospheric propagation, and target lethality. Among them, precision pointing of laser beam and high-bandwidth rejection of jitters produced by platform vibrations are one of the key technologies for the emerging fields of laser communications and HEL systems.</p> <p>HEL testbed has been developed to support the research environments on the precision beam control technology including acquisition, tracking, and pointing. The testbed incorporates optical table, two axis gimbal, high speed computers, and a variety of servo components, sensors, optical components, and software. In this report, system configuration and operation modes of the testbed are briefly introduced. The results of the experiments and integrated modeling from component to system level are described and discussed. Based on these results, new control algorithms are designed and it is shown that the algorithm can improve the pointing performance of the system.</p>				
14. SUBJECT TERMS High energy laser(HEL), beam control, fast steering mirror, 2 axis gimbal, stabilization, video tracking, feedforward control, adaptive filter.			15. NUMBER OF PAGES 78	
			16. PRICE CODE	
17. SECURITY CLASSIFICATION OF REPORT Unclassified	18. SECURITY CLASSIFICATION OF THIS PAGE Unclassified	19. SECURITY CLASSIFICATION OF ABSTRACT Unclassified	20. LIMITATION OF ABSTRACT UU	

THIS PAGE INTENTIONALLY LEFT BLANK

ABSTRACT

High energy laser (HEL) weapons are some of most challenging military applications in the future battle fields since the speed of light delivery enables the war fighter to engage very distant targets immediately. The issues of the technology on the HEL system include various types of high energy laser devices, beam control systems, atmospheric propagation, and target lethality. Among them, precision pointing of laser beam and high-bandwidth rejection of jitters produced by platform vibrations are one of the key technologies for the emerging fields of laser communications and HEL systems.

HEL testbed has been developed to support the research environments on the precision beam control technology including acquisition, tracking, and pointing. The testbed incorporates optical table, two axis gimbal, high speed computers, and a variety of servo components, sensors, optical components, and software. In this report, system configuration and operation modes of the testbed are briefly introduced. The results of the experiments and integrated modeling from component to system level are described and discussed. Based on these results, new control algorithms are designed and it is shown that the algorithm can improve the pointing performance of the system.

THIS PAGE INTENTIONALLY LEFT BLANK

TABLE OF CONTENTS

1.	INTRODUCTION	1
2.	HEL TESTBED	3
2.1.	CONFIGURATION.....	3
2.1.1.	Host computer.....	4
2.1.2.	Target computer	5
2.1.3.	Beam control system.....	7
2.2.	SYSTEM OPERATION MODE	9
2.2.1.	Init mode	10
2.2.2.	Emergency mode	13
2.2.3.	Normal control mode	13
2.2.4.	WFOV track mode.....	14
2.2.5.	NFOV track mode.....	15
3.	EXPERIMENTS.....	17
3.1.	WFOV CONTROL LOOP	18
3.1.1.	Resonance frequency	18
3.1.1.1.	Test scenario.....	19
3.1.1.2.	Test results.....	20
3.1.1.3.	Summary and discussion.....	28
3.1.2.	Rate loop servo bandwidth.....	29
3.1.2.1.	Test scenario.....	31
3.1.2.2.	Test results.....	31
3.1.2.3.	Summary and discussion.....	33
3.1.3.	Rate loop stabilization.....	33
3.1.3.1.	Test results.....	34
3.1.3.2.	Summary and discussion.....	35

3.2.	NFOV CONTROL LOOP	36
3.2.1.	Fast steering mirror	36
3.2.2.	NFOV bandwidth.....	37
4.	MODELING AND SIMULATION.....	40
4.1.	COMPONENT MODELING	40
4.1.1.	Gyro	40
4.1.2.	Power amplifier.....	41
4.1.3.	Fast steering mirror	43
4.1.4.	ALAR.....	44
4.1.5.	Limit.....	45
4.1.6.	Disturbance model	46
4.2.	WFOV CONTROL LOOP	46
4.2.1.	Rate control loop.....	47
4.2.2.	Position control loop.....	49
4.3.	NFOV CONTROL LOOP	50
4.4.	INTEGRATED CONTROL MODEL	51
5.	COMPENSATOR DESIGN	54
5.1.	FEED FORWARD CONTROL.....	54
5.2.	ADAPTIVE FILTER WITH F/F CONTROL	55
6.	RESULTS AND CONCLUSION.....	61
	INITIAL DISTRIBUTION LIST	63

LIST OF FIGURES

Figure 1. Picture of HEL testbed	3
Figure 2. System configuration.....	3
Figure 3. Control block diagram.....	4
Figure 4. An example of user interface.....	5
Figure 5. External interfaces of target computer	6
Figure 6. Schematic of beam control system.....	8
Figure 7. Breakdown list of beam control system	8
Figure 8. WFOV track loop	9
Figure 9. NFOV track loop.....	9
Figure 10. System operation modes and transition diagram.....	10
Figure 11. Mechanical limit switches	11
Figure 12. Transition diagram of Init Mode	12
Figure 13. Transition logic of Init Mode	12
Figure 14. Sinusoidal commutation logic	13
Figure 15. Transition diagram of WFOV track mode.....	14
Figure 16. Transition logic of WFOV track mode.....	15
Figure 17. Transition diagram of NFOV track mode	16
Figure 18. Transition logic of NFOV track mode.....	16
Figure 19. Experiment configuration.....	17
Figure 20. Test points of resonance frequency	18
Figure 21. Resonance analysis flow.....	18
Figure 22. Outliers in gyro signal	19
Figure 23. Torque input	20
Figure 24. Gyro output.....	20
Figure 25. PSD 1	21
Figure 26. PSD 2.....	21
Figure 27. Torque input	21

Figure 28. Gyro output.....	21
Figure 29. PSD 1.....	22
Figure 30. PSD 2.....	22
Figure 31. Torque input	22
Figure 32. Encoder output.....	22
Figure 33. PSD 1.....	23
Figure 34. PSD 2.....	23
Figure 35. Torque input	23
Figure 36. Encoder output.....	23
Figure 37. PSD 1.....	24
Figure 38. PSD 2.....	24
Figure 39. Torque input	24
Figure 40. Gyro output.....	24
Figure 41. Torque input	25
Figure 42. Gyro output.....	25
Figure 43. Torque input	25
Figure 44. Gyro output.....	25
Figure 45. PSD 1.....	26
Figure 46. PSD 2.....	26
Figure 47. Torque input	26
Figure 48. Encoder output.....	26
Figure 49. PSD 1.....	27
Figure 50. PSD 2.....	27
Figure 51. Torque input	27
Figure 52. Encoder output.....	27
Figure 53. PSD 1.....	28
Figure 54. PSD 2.....	28
Figure 55. Test point of servo bandwidth	29
Figure 56. Bandwidth analysis flow	29
Figure 57. Rate input.....	31

Figure 58. Gyro output.....	31
Figure 59. AZ transfer function	32
Figure 60. Rate input.....	32
Figure 61. Gyro output.....	32
Figure 62. EL transfer function.....	32
Figure 63. Test point of resonance.....	33
Figure 64. Disturbance input.....	34
Figure 65. Error output	34
Figure 66. AZ transfer function	34
Figure 67. Disturbance input.....	34
Figure 68. Error output	35
Figure 69. EL transfer function.....	35
Figure 70. Test point of FSM.....	36
Figure 71. AZ transfer function	34
Figure 72. EL transfer function.....	37
Figure 73. Test point of NFOV track loop.....	37
Figure 74. Test scheme of NFOV track loop.....	38
Figure 75. AZ transfer function	39
Figure 76. EL transfer function.....	39
Figure 77. Limit function.....	46
Figure 78. WFOV Simulink model.....	47
Figure 79. AZ step response	47
Figure 80. AZ transfer fuction	47
Figure 81. EL step response.....	48
Figure 82. EL transfer function.....	48
Figure 83. AZ step response	49
Figure 84. AZ transfer function	49
Figure 85. EL step response.....	49
Figure 86. EL transfer function.....	49
Figure 87. NFOV Simulink model	50

Figure 88. Step response	50
Figure 89. Frequency response	50
Figure 90. Integrated HEL model	51
Figure 91. Target motion	51
Figure 92. Rate of WFOV LOS	51
Figure 93. WFOV track error.....	52
Figure 94. NFOV track error	52
Figure 95. Disturbance input.....	52
Figure 96. Rate of WFOV LOS	52
Figure 97. WFOV track error.....	53
Figure 98. NFOV track error	53
Figure 99. WFOV track error.....	54
Figure 100. NFOV track error	54
Figure 101. WFOV track error.....	55
Figure 102. NFOV track error	55
Figure 103. Block diagram of adaptive filter.....	55
Figure 104. Detailed structure of the filter component.....	56
Figure 105. WFOV track error.....	57
Figure 106. NFOV track error	57
Figure 107. Convergence of filter coefficients	57
Figure 108. Learning curve of tracking errors for varying step size parameter	58
Figure 109. WFOV track error.....	59
Figure 110. NFOV track error	59
Figure 111. F/F control and adaptive filter	59
Figure 112. Error for target motion and disturbance	60

LIST OF TABLES

Table 1. PCI boards inside the target computer	7
Table 2. Init mode transition.....	11
Table 3. WFOV track mode transition.....	14
Table 4. NFOV track mode transition.....	15
Table 5. Scenario for resonance test	20
Table 6. Summary of resonance frequency.....	29
Table 7. Scenario for servo bandwidth test.....	31
Table 8. Scenario for stabilization test.....	33
Table 9. Scenario for FSM test	36
Table 10. Scenario for NFOV track loop test	38
Table 11. Summary of limit fuction.....	46
Table 12. Summary of WFOV parameters	49
Table 13. Summary of NFOV parameters	50
Table 14. Summary of system performance	61

THIS PAGE INTENTIONALLY LEFT BLANK

1. INTRODUCTION

High energy laser (HEL) weapons are ready for some of the most challenging military applications in future battle fields since speed of light delivery enables the war fighter to engage very distant targets immediately. The issues of the technology on HEL systems include various types of high energy laser devices, beam control systems, atmospheric propagation, and target lethality issues. Among them, precision pointing of laser beam and high-bandwidth rejection of jitters produced by platform vibrations are among the key technologies in the emerging fields of laser communications and HEL systems.

Optical beam control describes the centroid shifting of a laser on the target, and is a concern of engineers and scientists working with lasers and electro optical systems. Platform motion and optical component motion causes optical jitter, resulting in poor pointing accuracy, and blurred images. Even small level relative motion between mirrors and lenses can degrade the performance of precision pointing systems. Sources contributing to optical jitter include thermal effects, mechanical vibration, acoustics, static and dynamic loading, and heating and cooling systems.

The NPS HEL testbed has been developed to support research environments on the precision beam control technology including acquisition, tracking, and pointing. The testbed incorporates an optical table, two axis gimbal, high speed computers, and a variety of servo components, sensors, optical components, and software. In this report, overall configuration and operation modes of the testbed are briefly introduced. Results of experiments and integrated modeling from component to system level are described and discussed. Based on these results, new control algorithms are designed and it is shown that these algorithms can improve pointing performance of the system.

Section 2 describes major components of the HEL testbed including host computer, target computer, and beam control system. A hardware architecture, interfaces, and system operation are represented in detail for each component. Section 3 describes experiments used for system identification of dynamics and transfer functions required

for further modeling and control system improvement. In section 4, modeling from the major servo component to WFOV and NFOV control system are presented and simulation results are discussed. Section 5 describes the design results of the new controller, which consists of feed forward control and adaptive filter. Experimental results and conclusions are summarized in Section 6.

2. HEL TESTBED

The objective of the HEL testbed is to provide a research environment for the development of new technologies related with acquisition, pointing, tracking, and jitter control. A picture of the HEL testbed is shown in Figure 1.

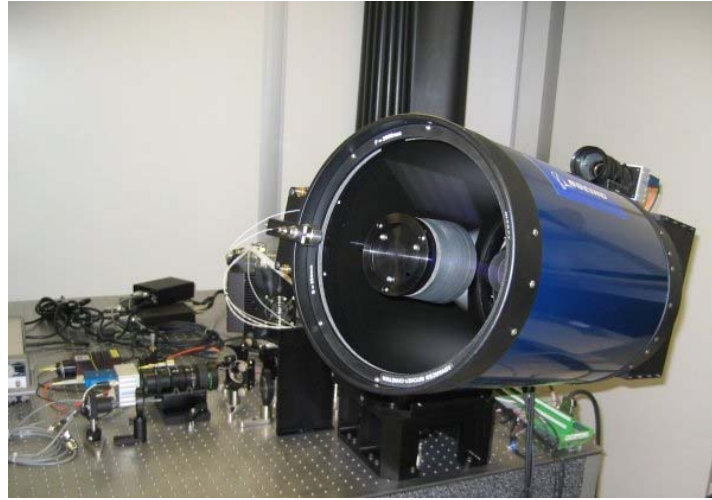


Figure 1. Picture of HEL testbed

2.1. Configuration

HEL testbed consists of three major components; host computer, target computer, and beam control system. A simple architecture of the testbed and control block diagram are shown in Figures 2 and 3.

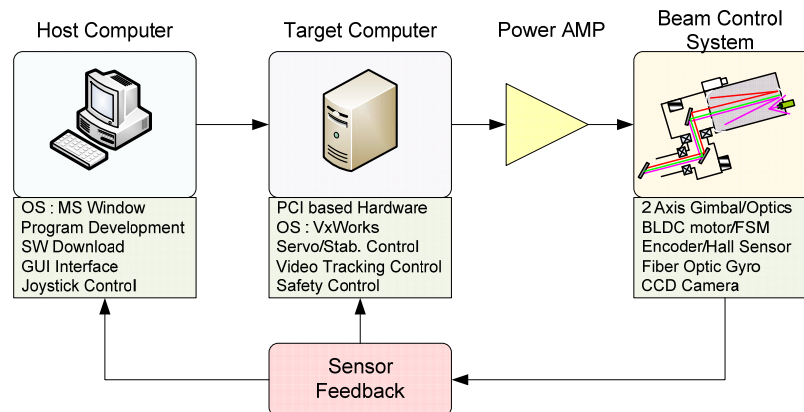


Figure 2. System configuration

The Host computer manages system operation modes and all sub-systems through user interfaces. A target computer executes real time codes and directly controls the beam control system. The main control loop consists of three feedback loops: two position control loops and one rate control loop as shown in Figure 3. Besides these main components, a moving target with illuminated light source also played an important role in evaluation of system performance.

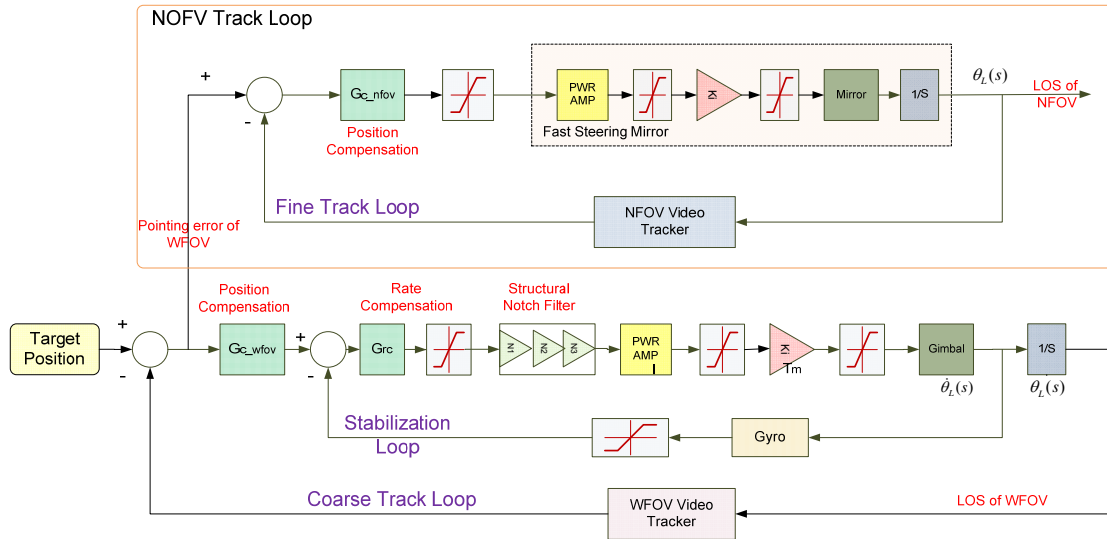


Figure 3. Control block diagram

2.1.1. Host computer

The host computer is a MS Windows based personal computer in which all the software is developed, compiled, debugged, and tested. Final object codes are downloaded to the target computer via Ethernet connection. A Two axis joystick is attached to the host computer and generates motion commands. System operation mode is controlled by switches on the joystick. Several redundant switches are added for further applications. Menu driven user interfaces are also implemented to control WFOV and NFOV video tracker parameters such as video mode, track mode, gate size, and selection of video tracking algorithm. One of the menus is shown in Figure 4.

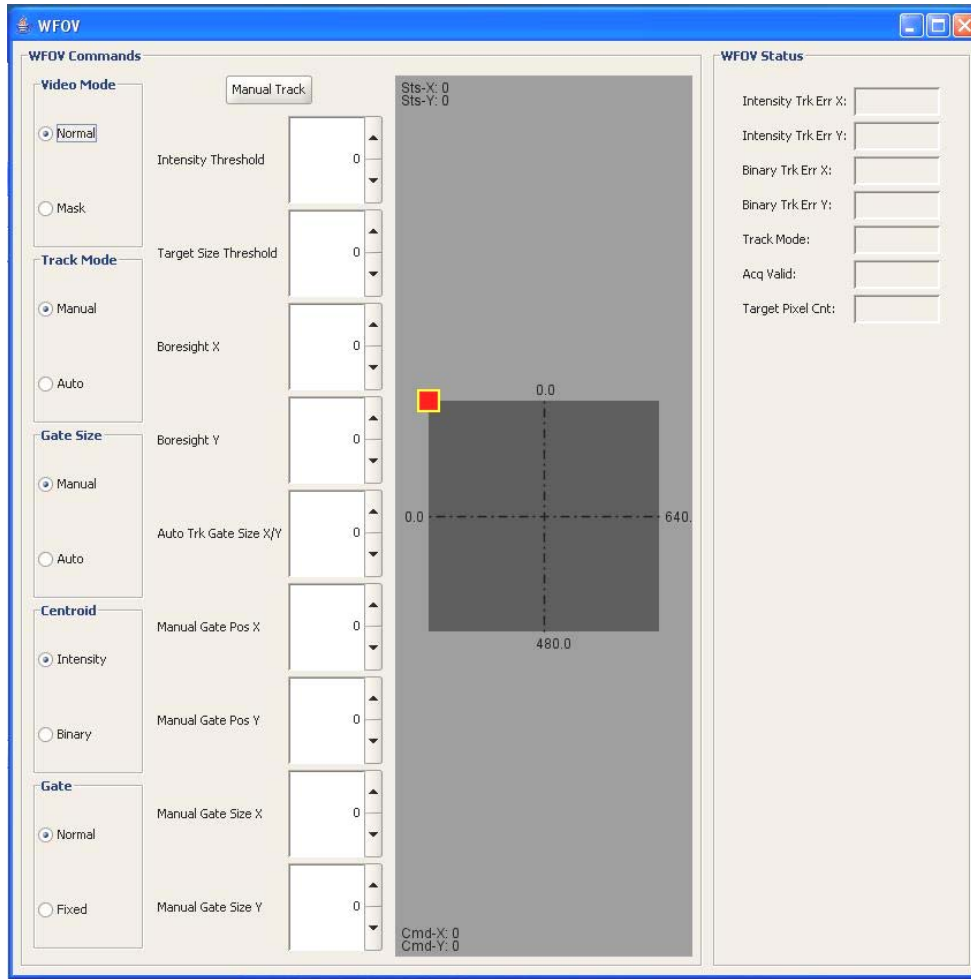


Figure 4. An example of user interface

2.1.2. Target computer

The Target computer is a Vxworks supported CompactPCI based system and consists of four 3U size boards: PowerPC compactPCI processor board(IMP2A), IO Pack Carrier board(ACPC8630), Multifunction CompactPCI board(ACPC730), and Counter Timer board(ACPC484). The PowerPC board mainly executes real time code and controls all the subsystems. A frame grabber PMC card is also mounted on the board to control and communicate with the WFOV and NOFV cameras which are connected by camera link. PowerPC board communicates with the Host computer by Ethernet from which it downloads SW codes and receives the control commands and uploads the

system status to the Host computer. An IO Pack carrier board has a PMC module which is connected to gyros by synchronous interface to control and receive angular rate data. The multifunction board is a precision CompactPCI board with the capability to monitor analog input signals. In addition, eight 16-bit analog voltage output channels and 16 digital input/output channels are provided and are connected to motor control command, FSM control command and various discrete signals. Lastly, rotary encoders providing relative positions are connected to the Counter Timer board. An External interface diagram of the target computer is presented in Figure 5 and characteristics of each board are summarized in Table 1.

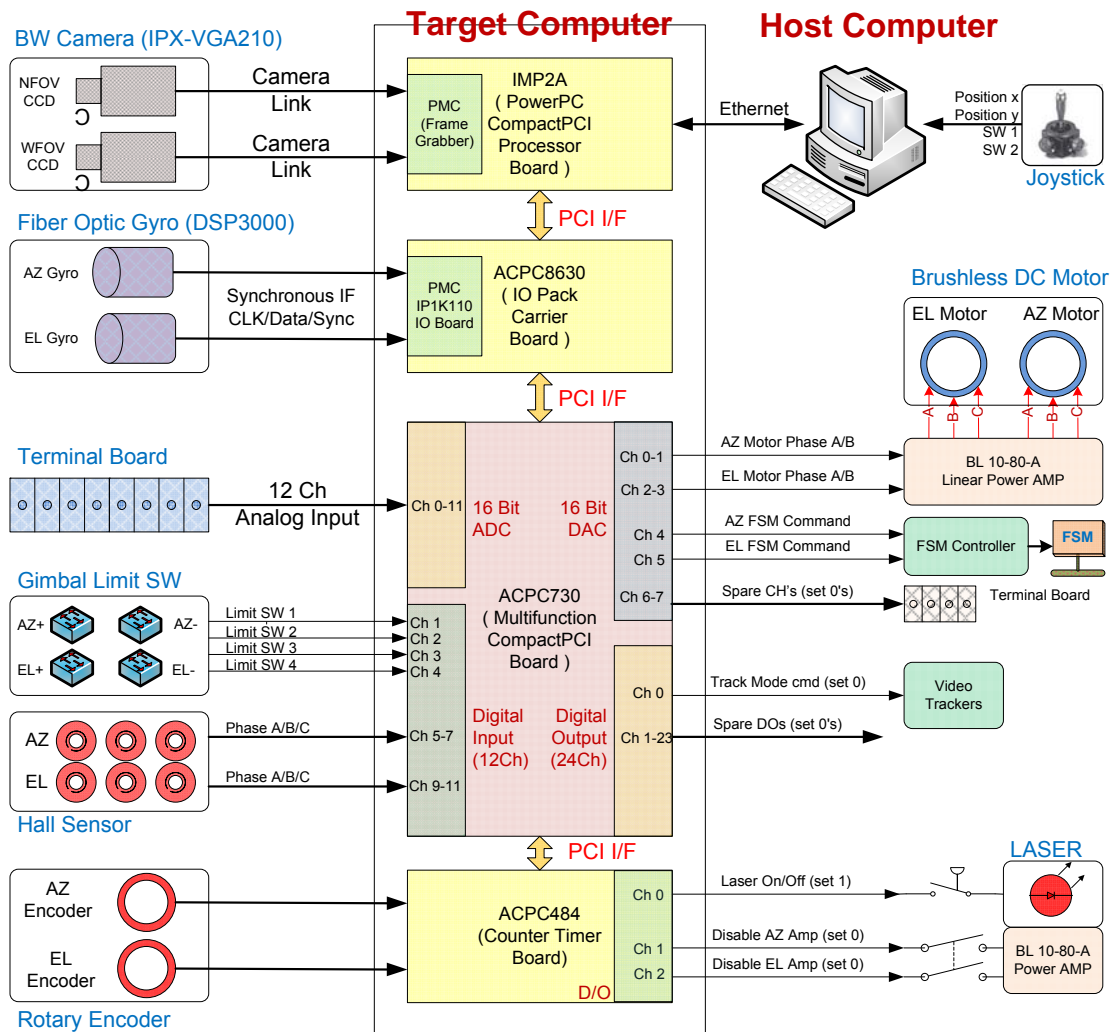


Figure 5. External interfaces of target computer

Table 1. PCI boards inside the target computer

Board type	Model	Characteristic
PowerPC board	IMP2A	<ul style="list-style-type: none"> • 1.4GHz PowerPC 7448, 3U CompactPCI SBC • 256 Mb SDRAM, 1Mb on-chip cache, 128Mb flash • 2 Ethernet, 2 serial ports, 4 bits GPIO • PCI-x capable PMC slot
IO Pack Carrier board	ACPC8630	<ul style="list-style-type: none"> • Carrier for Industrial I/O Pack Mezzanine board
Multifunction board	ACPC730	<ul style="list-style-type: none"> • 16 bit ADC : 16 differential or 32 single ended, 100KHz conversion rate (10uS conversion time) • 16 bit DAC : differential type, 80.8KHz conversion rate (12.375uS conversion time) • 32 bit Counter/Timer : waveform generation, event counting, watchdog timing, pulse width and period measurement • 16 Digital Input/Output channels
Counter Timer board	ACPC484	<ul style="list-style-type: none"> • Six 32 bit multifunction counter/timer : position measurement, pulse width modulation, watchdog timer, event counter, frequency measurement • 16 digital input/output channels

2.1.3. Beam control system

WFOV track loop, NFOV track loop, align and interface optics, and laser source are the major components of the beam control system whose schematic and breakdown list are shown in Figures 6 and 7. The WFOV track loop consists of two feedback control loops, inner loop and outer loop as shown in Figure 8. Inner loop is a rate control loop composed of gimbal, power amplifier, controller, and servo components (gyro, motor, and encoder). The rate loop accurately maintains line of sight (LOS) to the target in the inertial space with respect to external disturbances and tracks input rate commands generated from the WFOV tracker. Outer loop is a position control loop which consists of the WFOV camera and video tracking algorithm. It computes the error between LOS and the center of target, and sends the error signal to the rate command of the inner control loop.

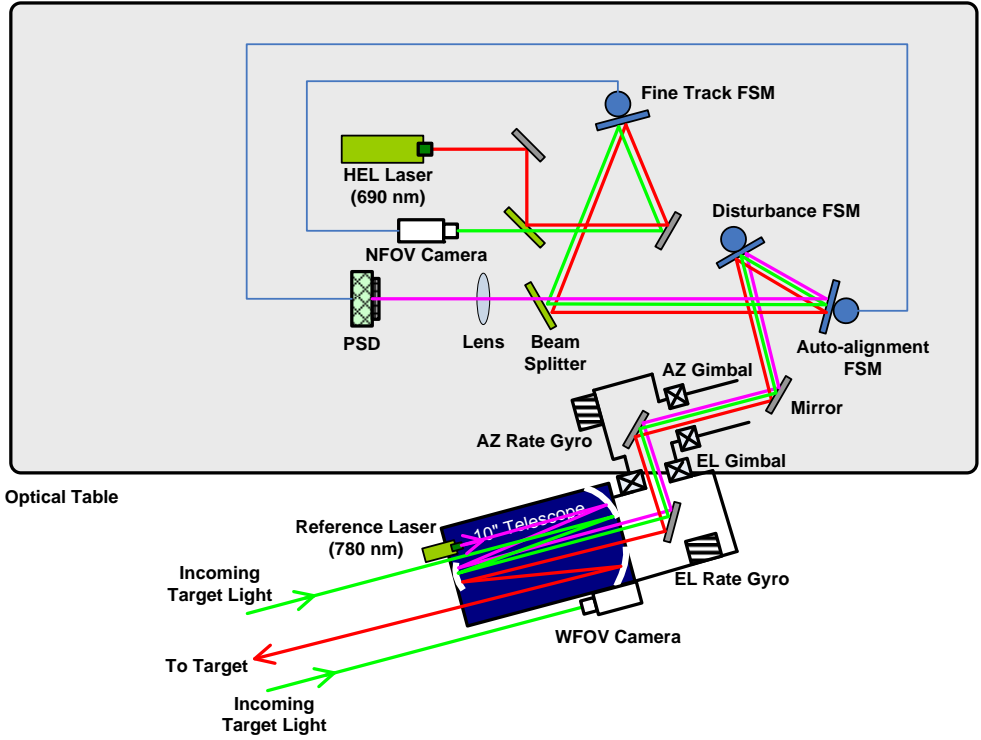


Figure 6. Schematic of beam control system

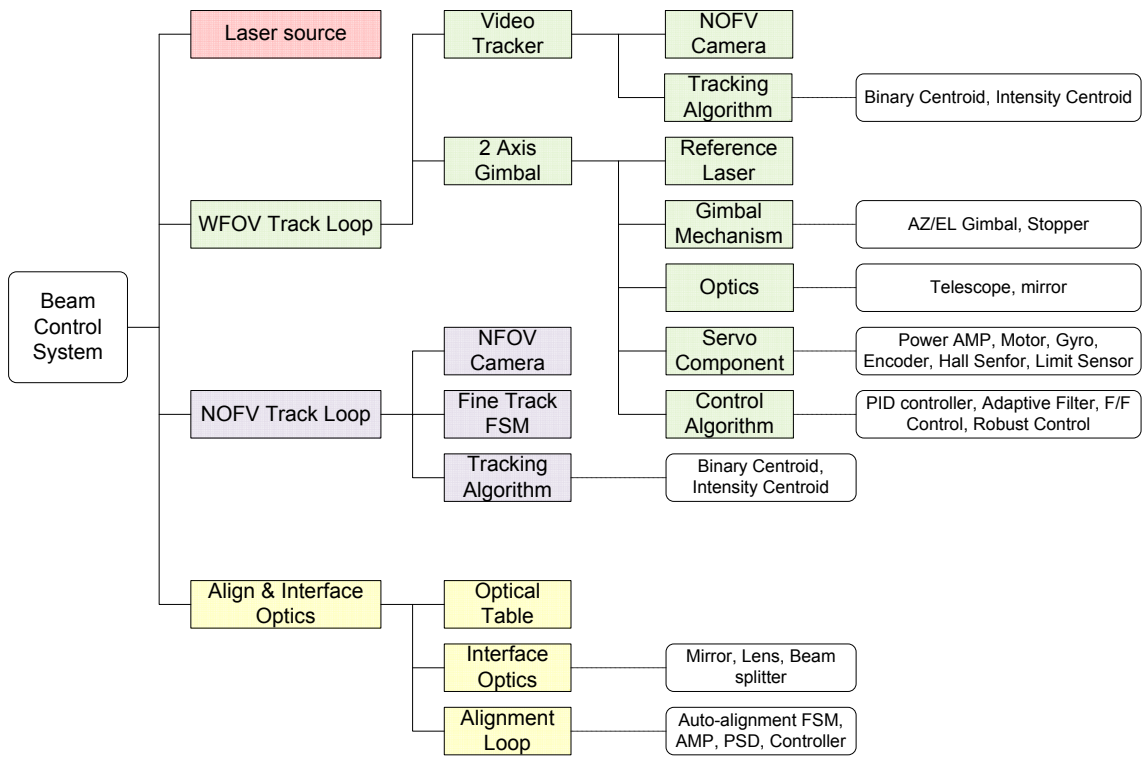


Figure 7. Breakdown list of beam control system

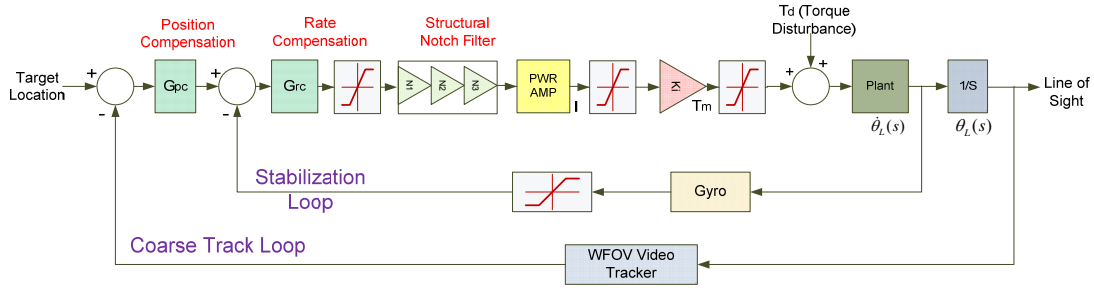


Figure 8. WFOV track loop

The NFOV track loop is a position control loop composed of a NFOV camera, Fast steering mirror(FSM), and video tracking algorithm as shown in Figure 9. The track loop detects errors that the WFOV track loop couldn't compensate and controls the LOS to minimize the pointing error between the target and LOS.

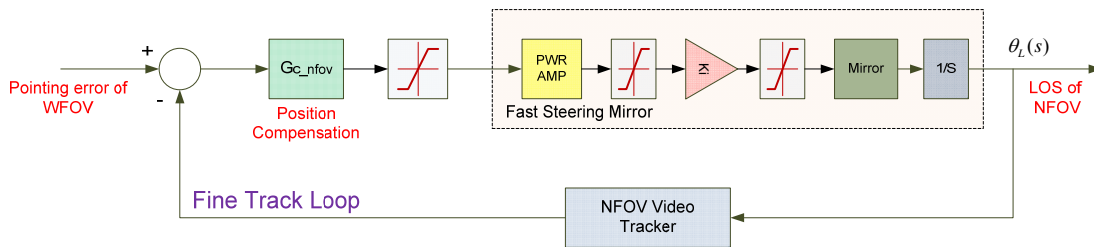


Figure 9. NFOV track loop

Several optical components such as mirrors, lens, and beam splitters are mounted on the optical table to make optical path from/to laser source, target, and sensors. An auto alignment control loop continuously detects an optical misalign between a reference laser and position sensitive device(PSD) sensor and realigns the optical path.

2.2. System operation mode

At power up, the system defaults to the 'Init Mode' in which the two axis gimbal moves from positive to negative mechanical limit position for encoder calibration. After system initialization, the power amplifier is operated in sinusoidal commutation mode and the system automatically switches to 'Normal Control Mode'. In this mode, rate commands from the joystick are enabled and the two axis gimbal is stabilized and

controlled in rate command. During the ‘Normal Control Mode’, proper menu selection on the host computer changes the system from ‘WFOV Track Mode’ to ‘NFOV Track Mode’. In order to protect the system from an abrupt motion due to abnormal operation or malfunction, over current is monitored in the power amplifier which automatically switches the changes system to ‘Emergency Mode’. Whole system operation mode and transition diagram are shown in Figure 10.

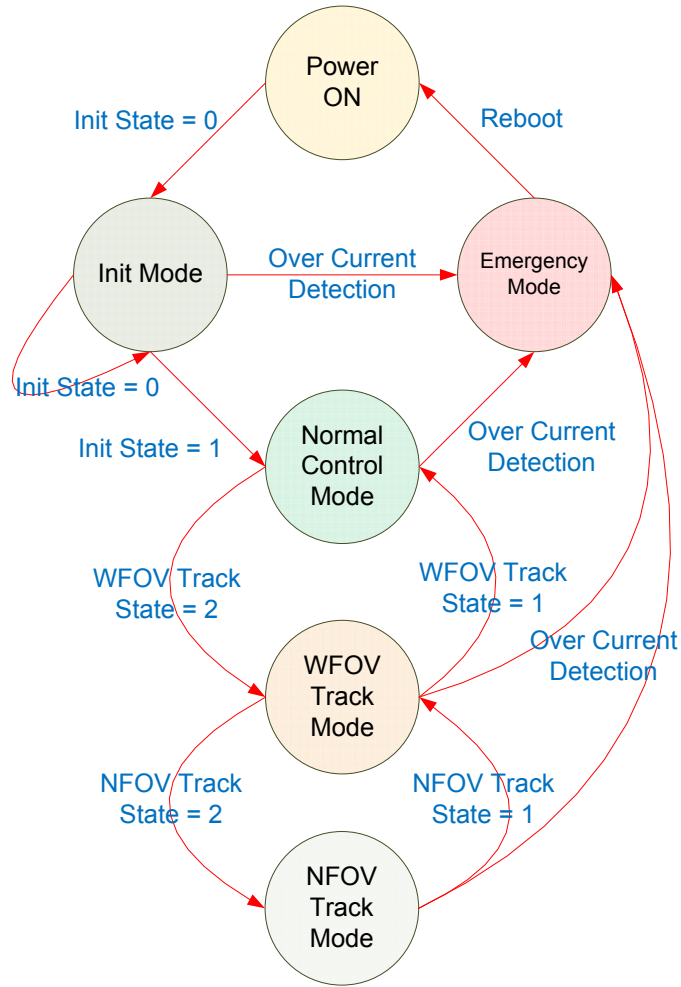


Figure 10. System operation modes and transition diagram

2.2.1. Init mode

Six step commutation based on the hall sensors is robust for motor control but increases motor torque ripple which reduces system pointing performance. In the normal

operation of the HEL system, sinusoidal commutation is implemented by using relative encoder to minimize the motor torque ripple for maximum accuracy. However, the sinusoidal commutation requires encoder calibration before normal operation. In order to do this, system SW performs an initialization process at power up. During the ‘Init Mode’, the servo controller is working in the six step commutation mode for a short time using the 6 motor hall sensors and determines the offset between the actual motor angle and the measured motor angle. Four mechanical limit switches, 2 for AZ axis and 2 for EL axis, are installed on the testbed to measure the encoder offset, which are shown in Figure 11. Each switch output goes ‘High’ when the gimbal passes through the limit position. The transition logic from ‘Init Mode’ to ‘Normal Control Mode’ is described in Table 2 and a transition diagram is shown in Figures 12 and 13.

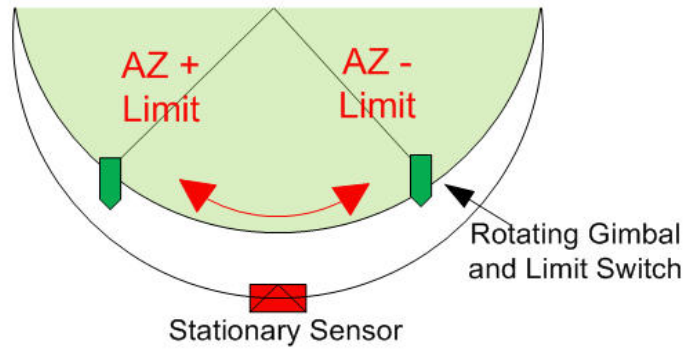


Figure 11. Mechanical limit switches

Table 2. Init mode transition

State No.	Switch Input				Internal State				Output (Init state)	Mode
	SW1 (AZ+)	SW2 (AZ-)	SW3 (EL+)	SW4 (EL-)	AZ init cmd	EL init cmd	Out1	Out2		
S0	0	0	0	0	0.375	0.375	2	2	0	Init Mode
S1	0	0	0	1	0.375	0.375	2	2	0	
S2	0	0	1	0	0.375	-0.375	2	2	0	
S3	0	0	1	1	0.375	0	2	3	0	
S4	0	1	0	0	0.375	0.375	2	2	0	
S5	0	1	0	1	0.375	0.375	2	2	0	
S6	0	1	1	0	0.375	-0.375	2	2	0	
S7	0	1	1	1	0.375	0	2	3	0	

S8	1	0	0	0	-0.375	0.375	2	2	0	
S9	1	0	0	1	-0.375	0.375	2	2	0	
S10	1	0	1	0	-0.375	-0.375	2	2	0	
S11	1	0	1	1	-0.375	0	2	3	0	
S12	1	1	0	0	0	0.375	3	2	0	
S13	1	1	0	1	0	0.375	3	2	0	
S14	1	1	1	0	0	-0.375	3	2	0	
S15	1	1	1	1	0	0	3	3	1	Normal mode

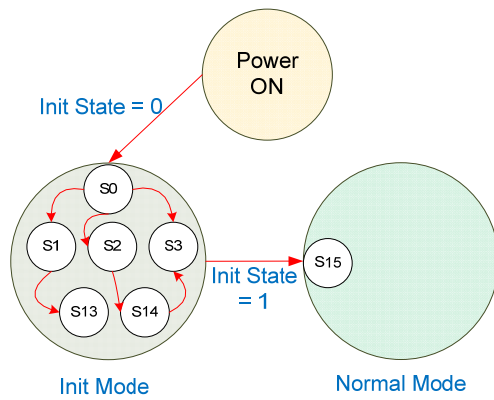


Figure 12. Transition diagram of Init Mode

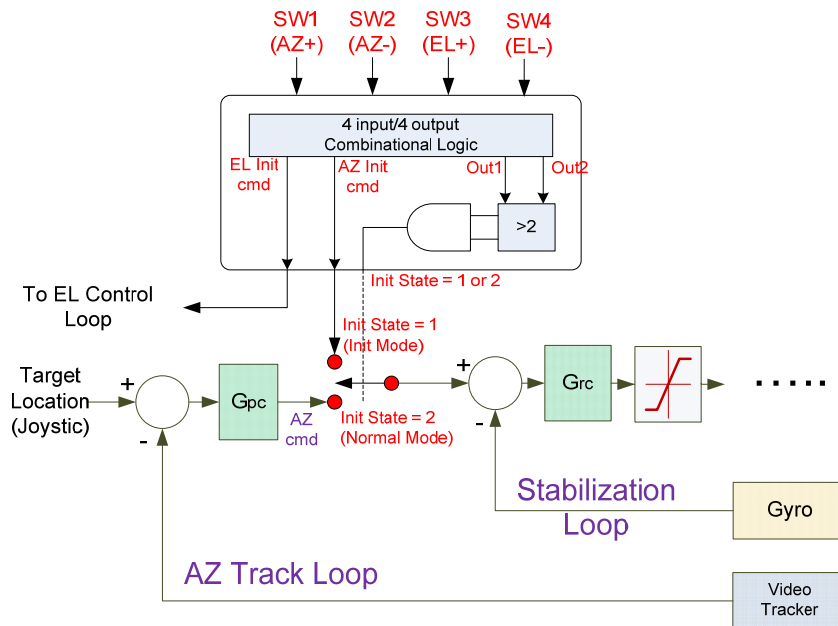


Figure 13. Transition logic of Init Mode

2.2.2. Emergency mode

Two brushless (BL) series linear amplifiers are adapted to drive a 2 axis gimbal. The BL drives features self-commutation with analog or digital Hall sensor feedback signals. Each drive is fully protected against over current. During the operation, if an over current condition is detected the power amplifier is shut down and the system goes into ‘Emergency Mode’. In order to get the system recovered from emergency mode, power should be reapplied to the power amplifier.

2.2.3. Normal control mode

After the ‘Init Mode’, the system automatically switches to ‘Normal Control Mode’. In normal mode, control torque commands are converted into two sinusoidal current commands based on the motor electrical angle with a 120 degree phase difference. The result is a high resolution commutation command precisely matched to the motor’s actual winding dynamics. The motor electrical angle is computed by multiplying the encode angle measurement by the number of motor pole pairs. These are shown in Figure 14.

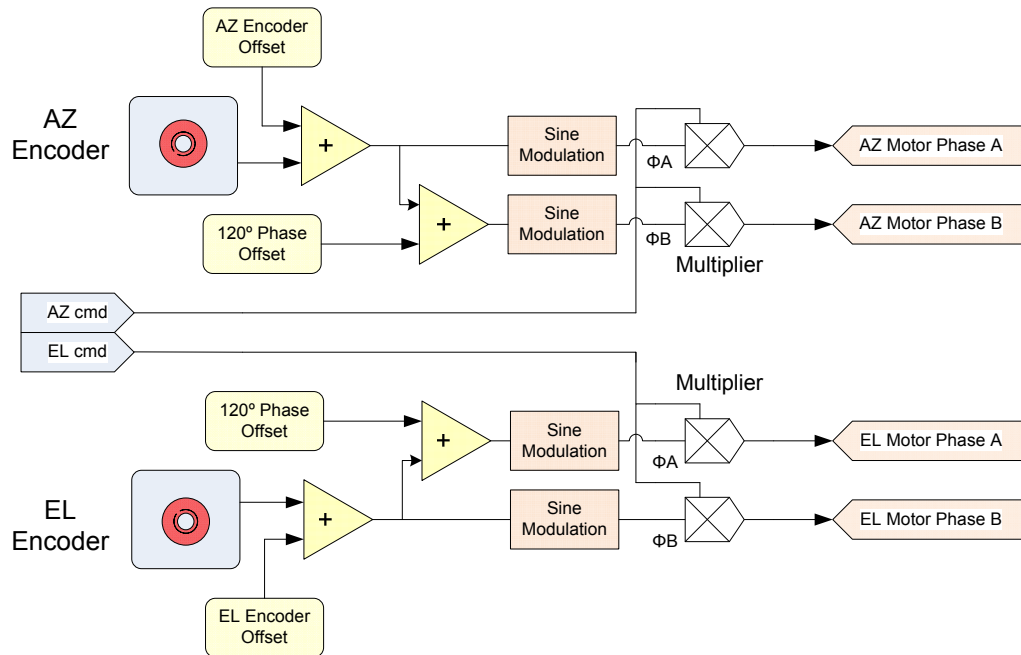


Figure 14. Sinusoidal commutation logic

2.2.4. WFOV track mode

A WFOV CCD camera is mounted on the gimbal and a video tracking algorithm calculates the errors between gimbal LOS and the center of target. The tracker supplies the error signal to the angular rate control loop and maintains the LOS on the center of target. System SW checks three logic signals, two from the video track algorithm and one from the joystick handle to determine if the system should stay in ‘Normal Control Mode’ or switch to ‘WFOV Track Mode’. Transition logic and block diagrams are shown in Table 3 and Figures 15-16 respectively.

Table 3. WFOV track mode transition

State No.	Input			WFOV Track state
	Joystick SW2	WFOV track acqValid	WFOV track Mode	
S0	0	0	0	1
S1	0	0	1	1
S2	0	1	0	1
S3	0	1	1	1
S4	1	0	0	1
S5	1	0	1	1
S6	1	1	0	1
S7	1	1	1	2

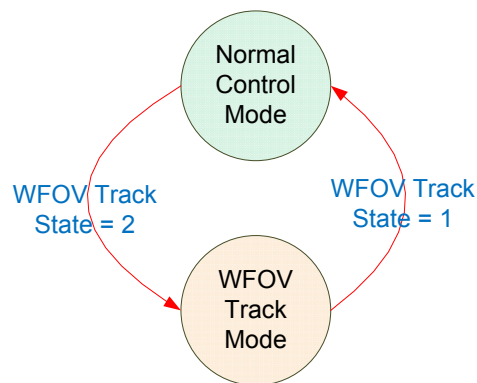


Figure 15. Transition diagram of WFOV track mode

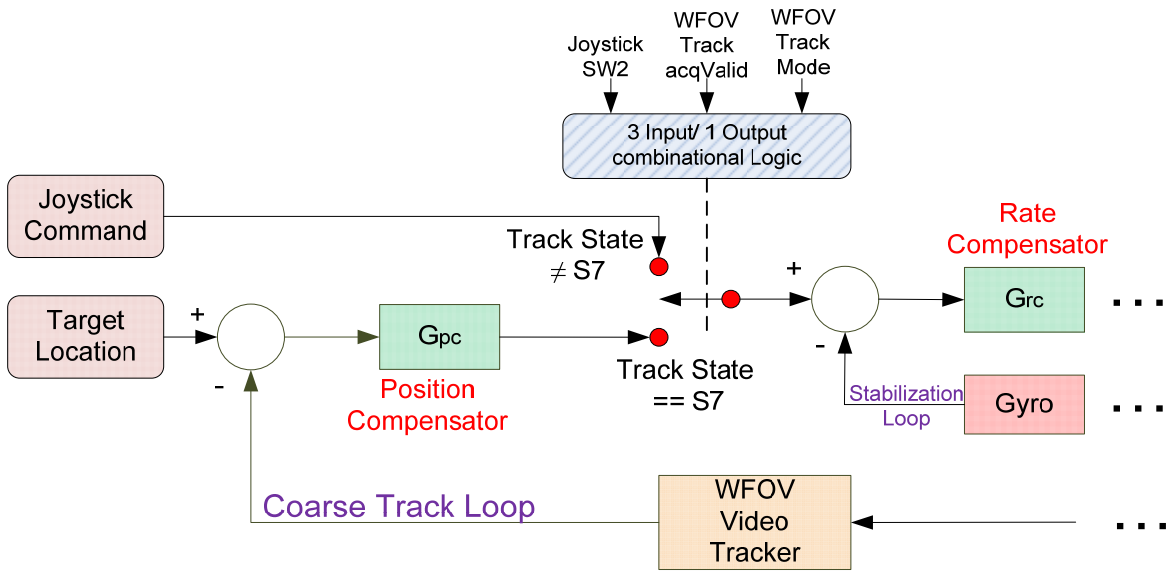


Figure 16. Transition logic of WFOV track mode

2.2.5. NFOV track mode

Transition condition to ‘NFOV Track Mode’ is nearly identical to ‘WFOV Track Mode’ except the transition occurs only between WFOV track mode and NFOV track mode. Transition logic and block diagrams are shown in Table 4 and Figures 17-18.

Table 4. NFOV track mode transition

State No.	Input			NFOV Track state
	Joystick SW1	NFOV track acqValid	NFOV track Mode	
S0	0	0	0	1
S1	0	0	1	1
S2	0	1	0	1
S3	0	1	1	1
S4	1	0	0	1
S5	1	0	1	1
S6	1	1	0	1
S7	1	1	1	2

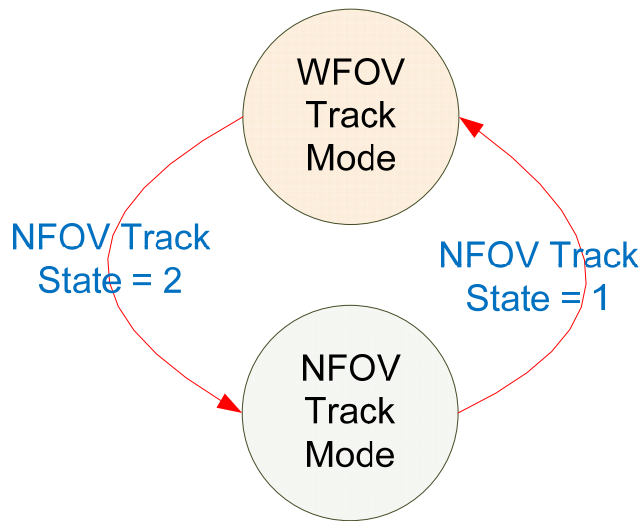


Figure 17. Transition diagram of NFOV track mode

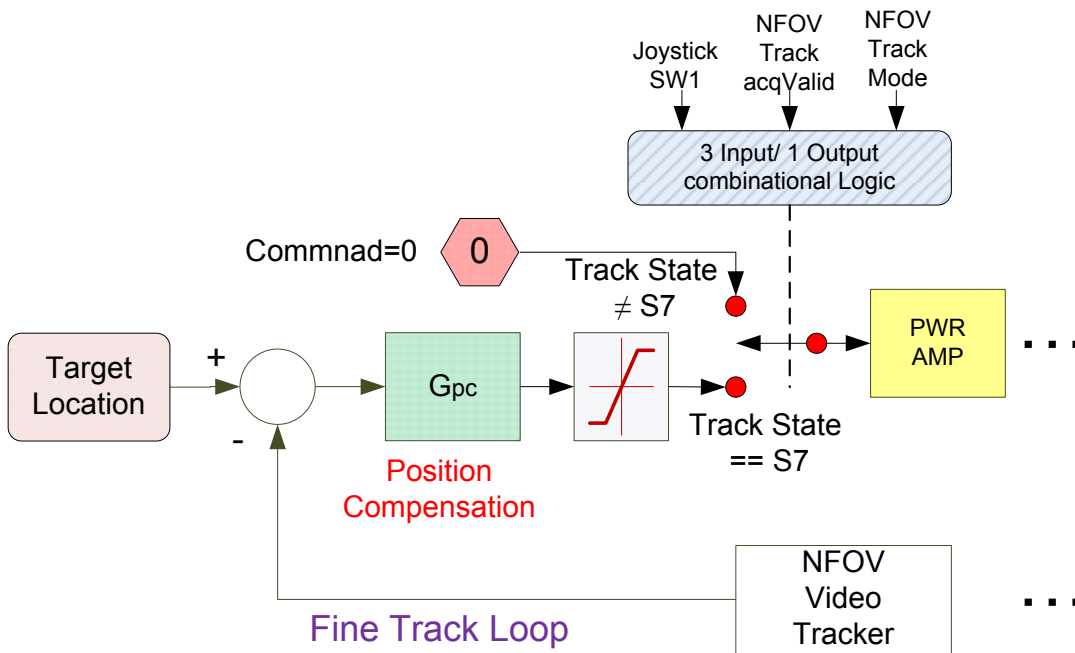


Figure 18. Transition logic of NFOV track mode

3. EXPERIMENTS

Several types of experiments were performed to determine characteristics of the HEL testbed, and the results of the tests were utilized for system modeling. The experiments included resonant frequency test, rate loop servo bandwidth and stabilization test, FSM test, and NFOV bandwidth test. Test configuration is shown in Figure 19. The target computer has an external terminal board which interfaces all the signals between the beam control system and target computer, and provides input/output test points. Test equipments such as dynamic signal analyzer, data acquisition system, and oscilloscope are used for signal generation, data storage, and observation of test signals.

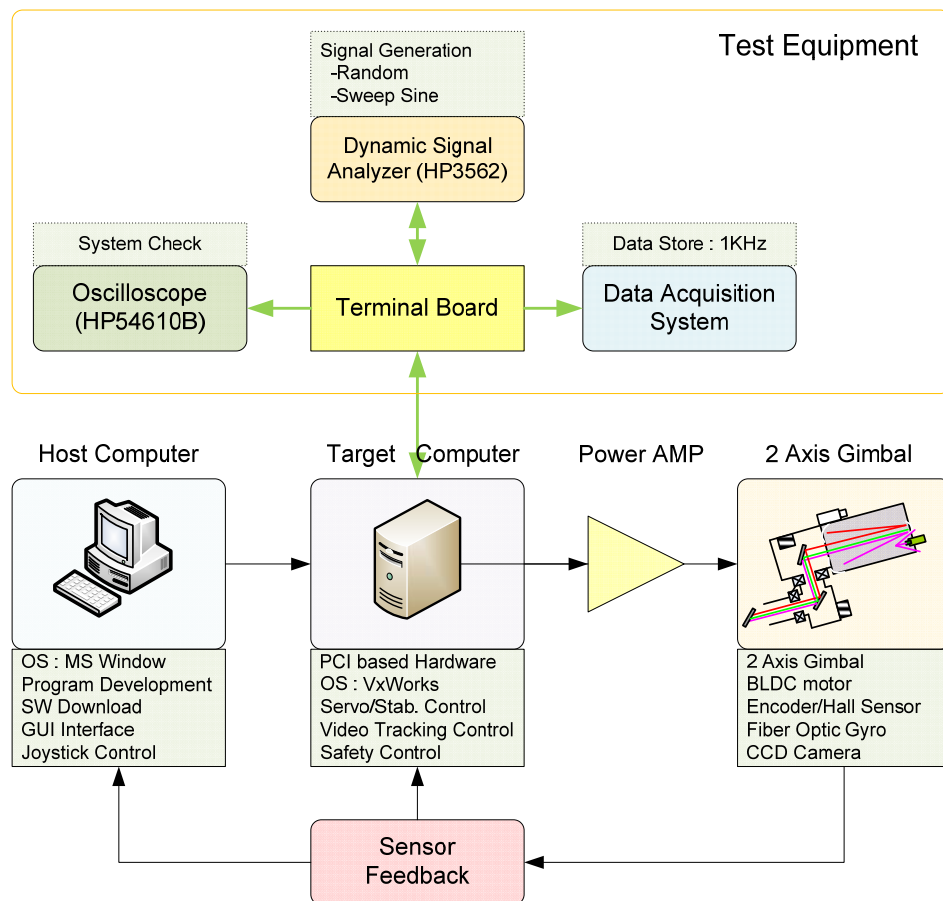


Figure 19. Experiment configuration

3.1. WFOV control loop

3.1.1. Resonance frequency

Random signals were applied to the power amplifier and output signals were picked up from gyro and encoder respectively. Test input and output points are shown in Figure 20. Data analysis flow for resonance frequency determination is shown in Figure 21. Power spectral density analysis of the measured data was used to calculate resonance frequencies.

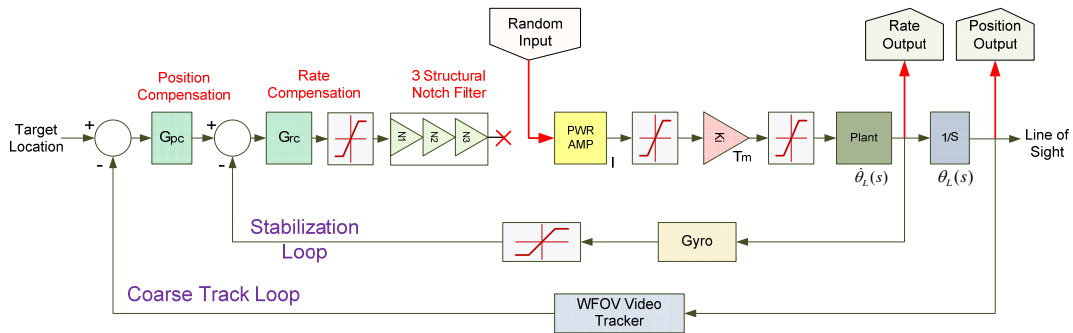


Figure 20. Test points of resonance frequency

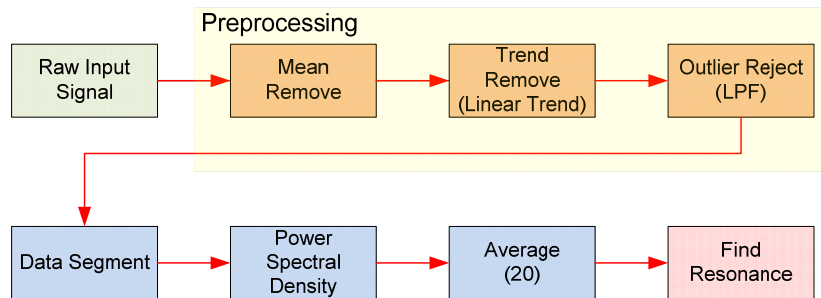


Figure 21. Resonance analysis flow

- Preprocessing

Preprocessing was applied before computing the power spectral density. Test data may have a constant offset or drift so, removing a trend from the data enables one to focus the analysis on fluctuation in the data. The mean and trend removal computes the least square fit of a straight line to the data and subtracts the resulting

function from the data. Malfunctions can also produce errors in measured values, called outliers. Such outliers might be caused by signal spikes or measurement malfunctions. If the outliers are not removed, this can adversely affect the estimated models. An example of outliers in gyro data is shown in Figure 22.

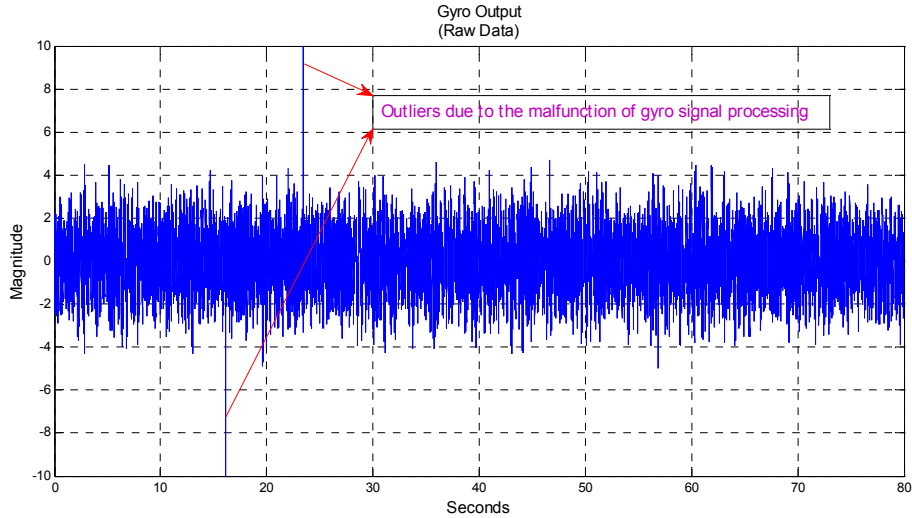


Figure 22. Outliers in gyro signal

- Power spectral density and averaging.

A Periodogram was chosen for power spectral density computation. For a data sequence $[x_1, x_2, \dots, x_n]$, a periodogram is given by the following formula and this expression forms an estimate of a signals' PSD:

$$S(e^{j\omega}) = \frac{1}{n} \left| \sum_{k=1}^n x_k e^{-j\omega k} \right|^2$$

In order to suppress spectral noises, PSD data was averaged 20 times.

3.1.1.1. Test scenario

Random signals were applied to the test input point with a magnitude of 1-2V. Frequency range of measured data was 0-100Hz, and 0-200Hz. Output data are from gyro and encoder is shown in Table 5.

Table 5. Scenario for resonance test

Dir.	Input (Vpeak)	Output Data	Time Length (sec)	Measured Data Analysis	
				Freq. Range (Hz)	Average No.
EL	1.0	Gyro	8	0-100	20
	1.0	Gyro	4	0-200	20
	1.0	Encoder	8	0-100	20
	1.0	Encoder	4	0-200	20
AZ	1.0	Gyro	8	0-100	20
	1.0	Gyro	4	0-200	20
	2.0	Encoder	8	0-100	20
	2.0	Encoder	4	0-200	20

3.1.1.2. Test results

For each axis, torque input and gyro/encoder output signals are plotted in the time domain and power spectral density of the output is depicted in the Figure 23-54.. PSD1 and PSD2 are the figures of the same power spectral density function. PSD2 is an enlarged plot of PSD1 around the low magnitude region to see resonance frequencies which have small magnitude.

- AZ gyro : frequency range is 0-100Hz

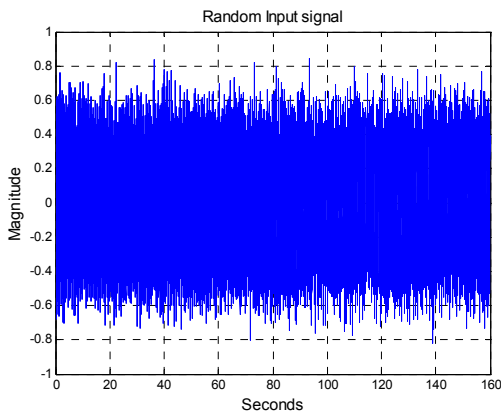


Figure 23. Torque input

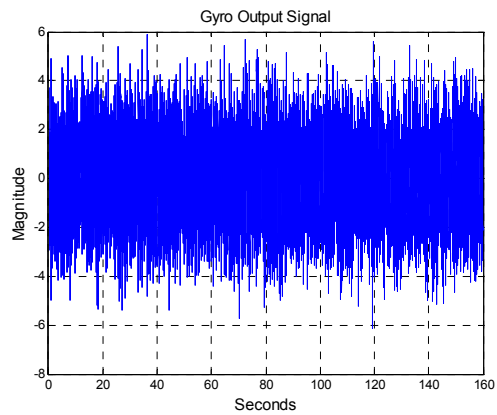


Figure 24. Gyro output

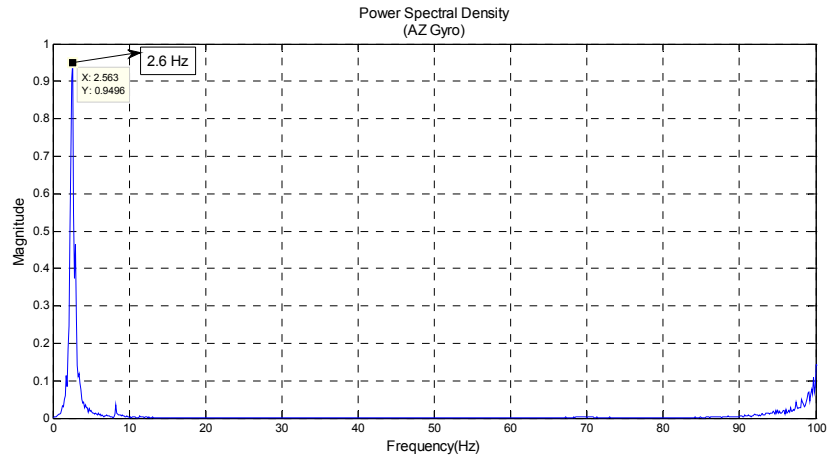


Figure 25. PSD 1

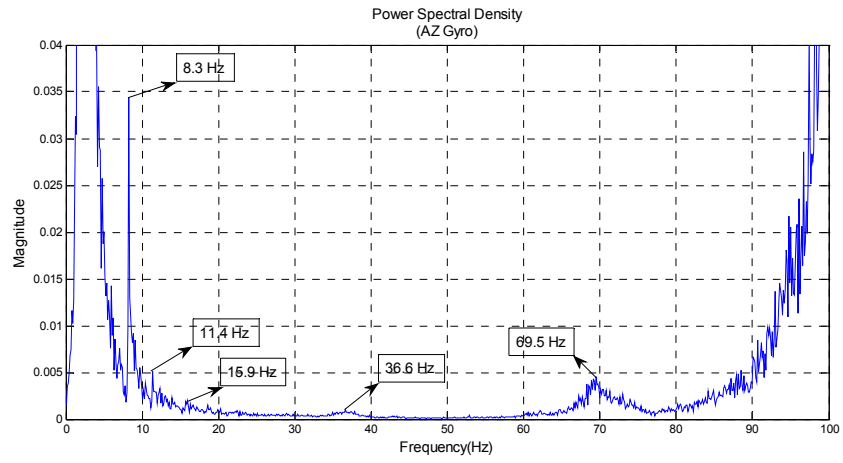


Figure 26. PSD 2

- AZ gyro : frequency range is 0-200Hz

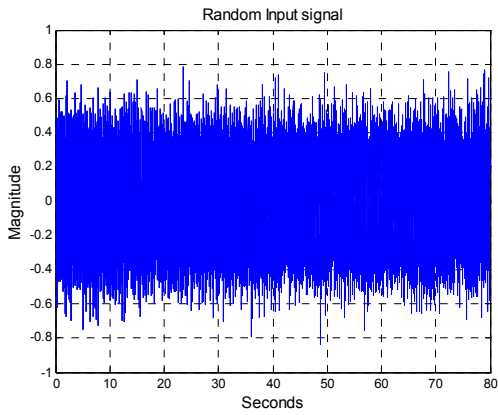


Figure 27. Torque input

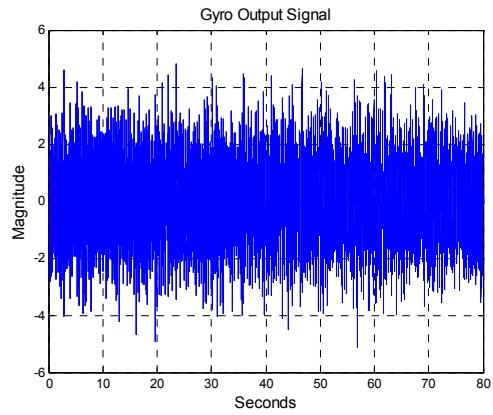


Figure 28. Gyro output

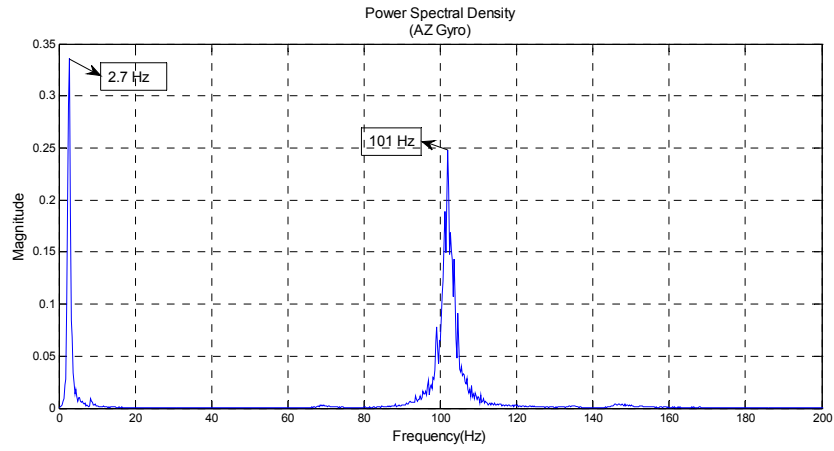


Figure 29. PSD 1

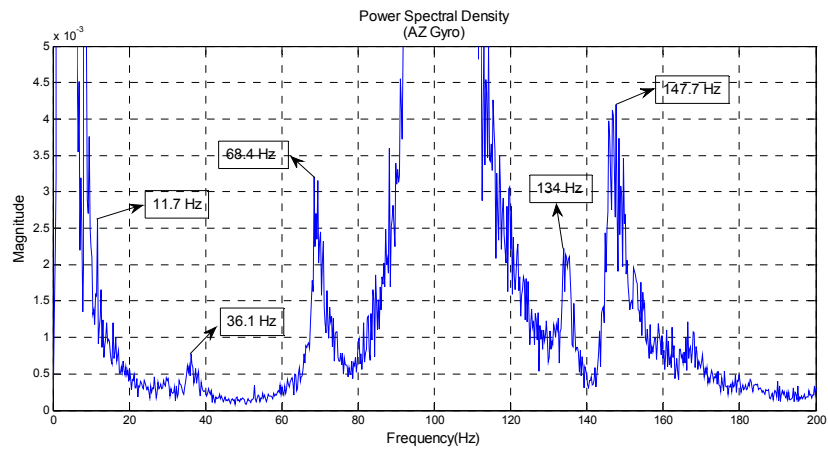


Figure 30. PSD 2

- AZ encoder : frequency range is 0-100Hz

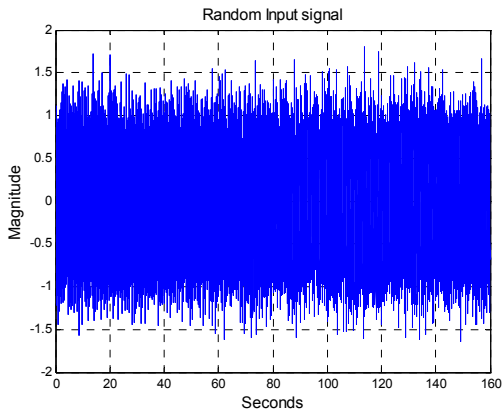


Figure 31. Torque input

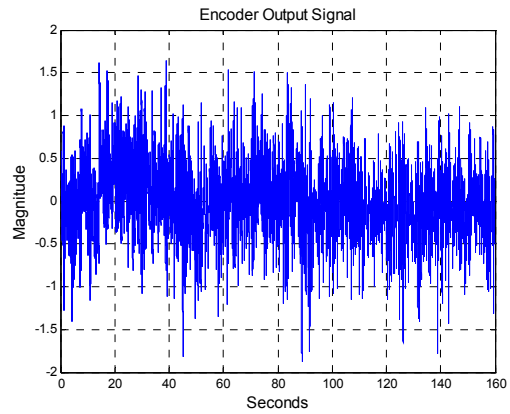


Figure 32. Encoder output

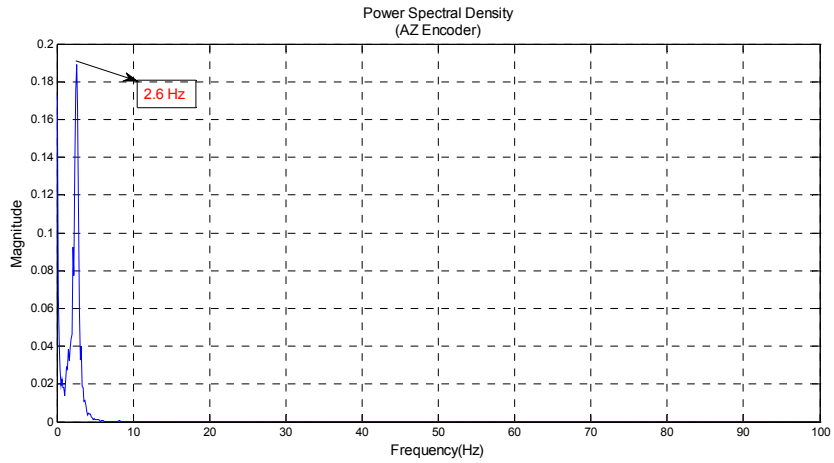


Figure 33. PSD 1

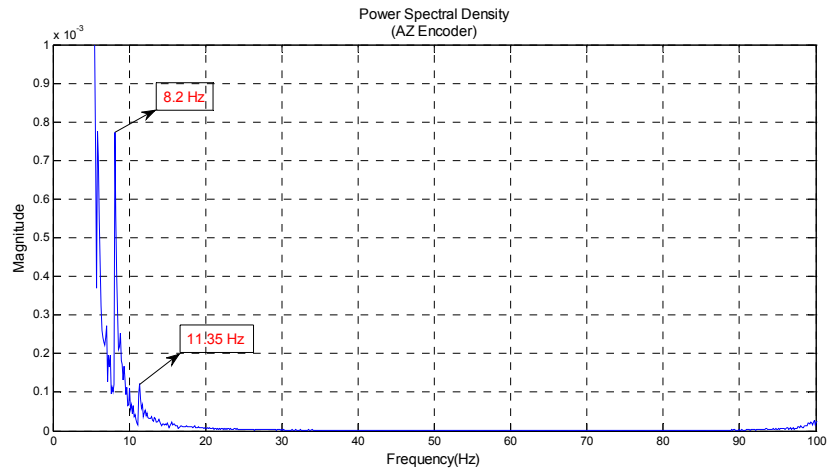


Figure 34. PSD 2

- AZ encoder : frequency range is 0-200Hz

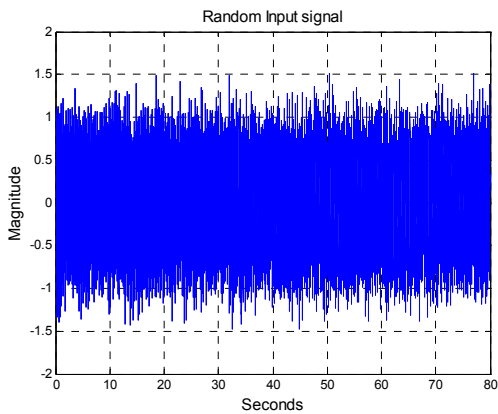


Figure 35. Torque input

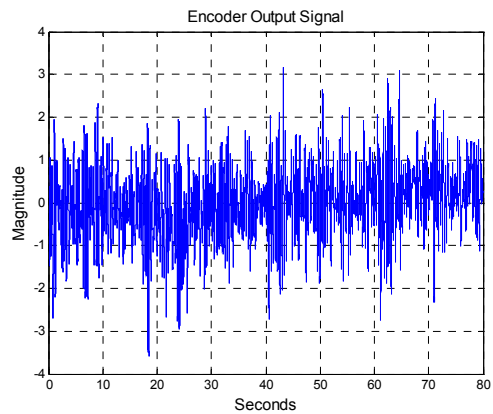


Figure 36. Encoder output

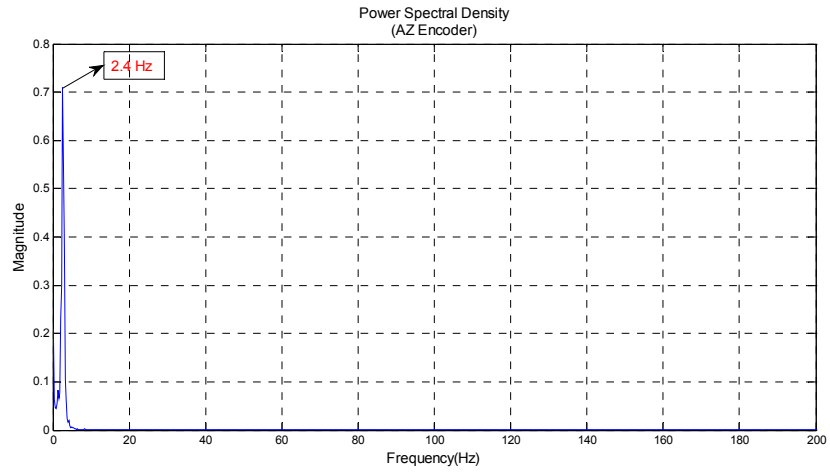


Figure 37. PSD 1

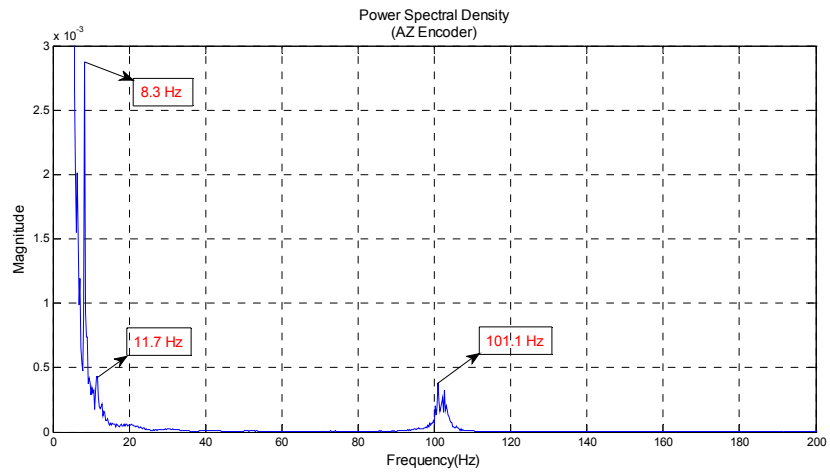


Figure 38. PSD 2

- EL gyro : frequency range is 0-100Hz

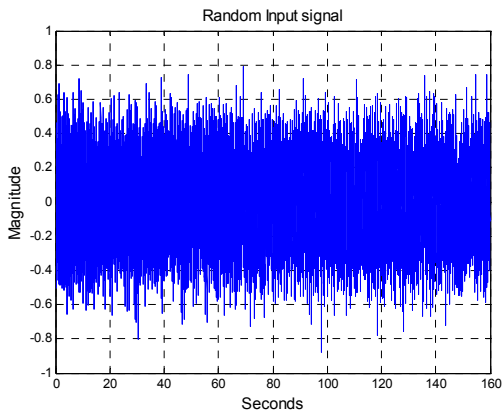


Figure 39. Torque input

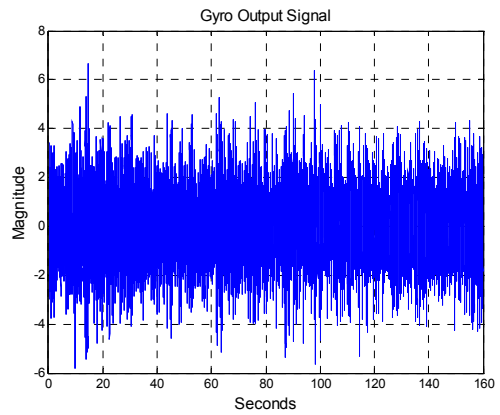


Figure 40. Gyro output

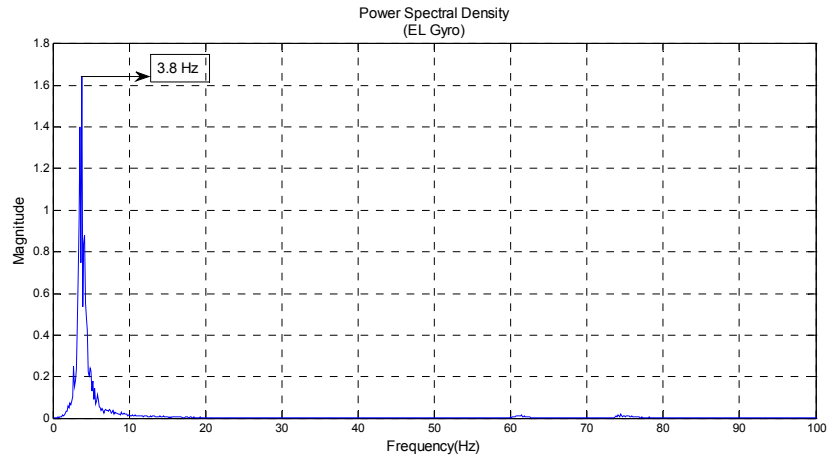


Figure 41. Torque input

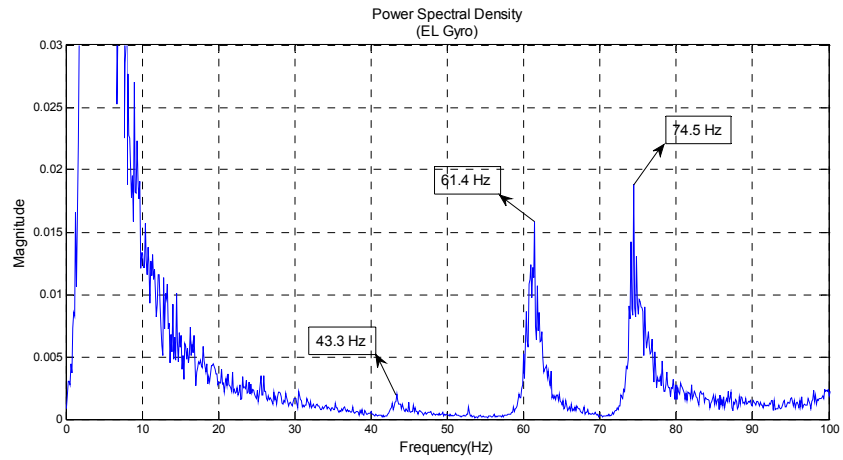


Figure 42. Gyro output

- EL gyro : frequency range is 0-200Hz

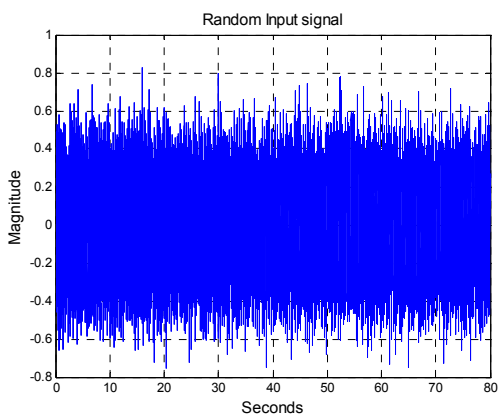


Figure 43. Torque input

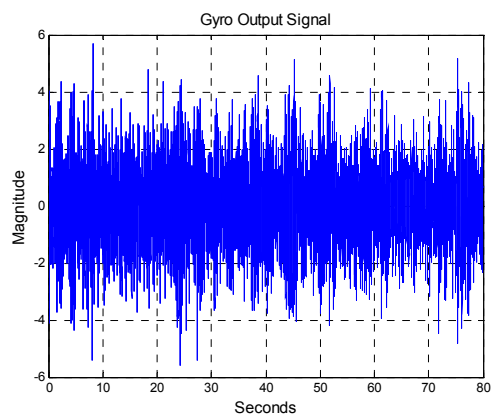


Figure 44. Gyro output

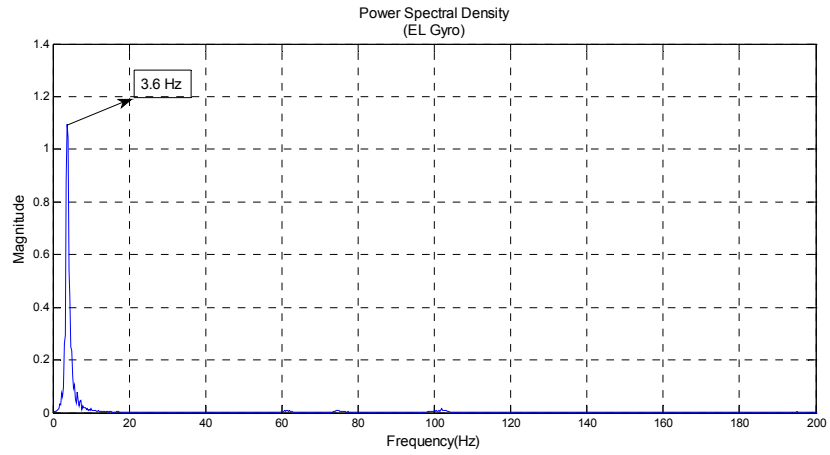


Figure 45. PSD 1

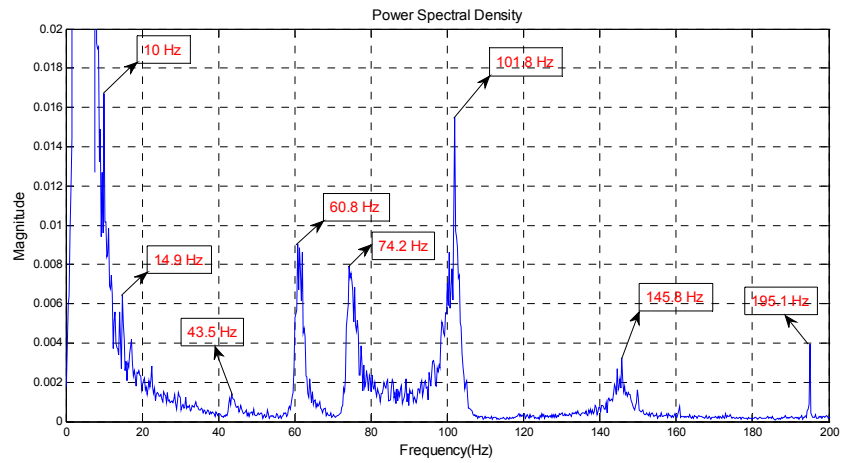


Figure 46. PSD 2

- EL encoder : frequency range is 0-100Hz

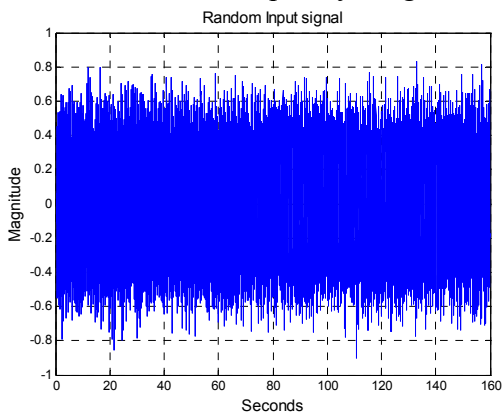


Figure 47. Torque input

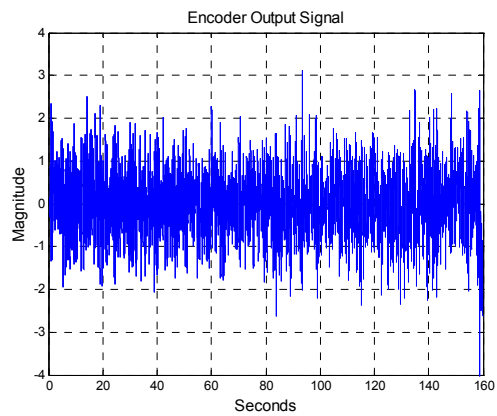


Figure 48. Encoder output

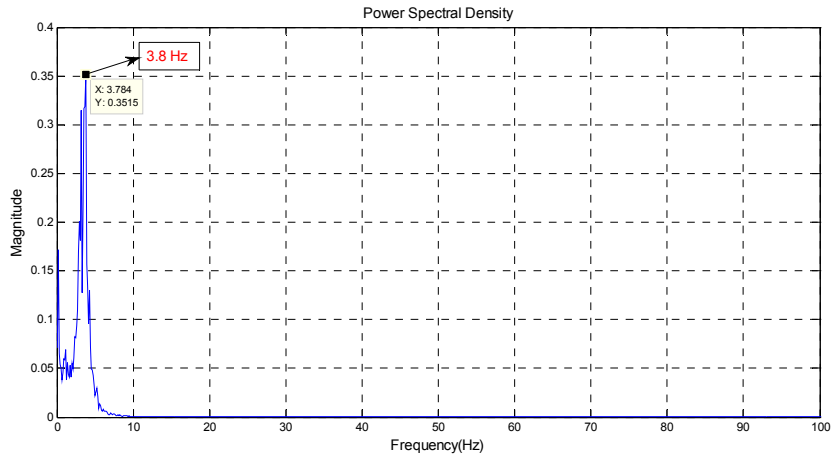


Figure 49. PSD 1

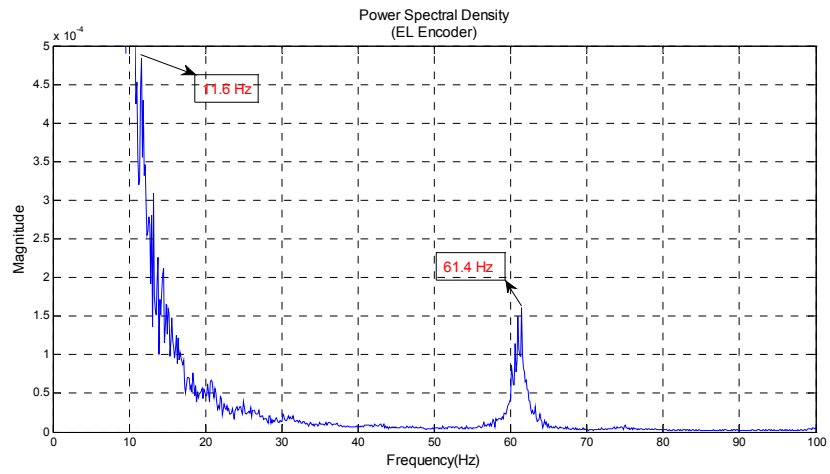


Figure 50. PSD 2

- EL encoder : frequency range is 0-200Hz

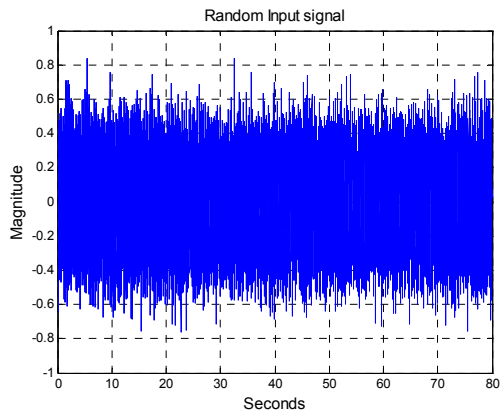


Figure 51. Torque input

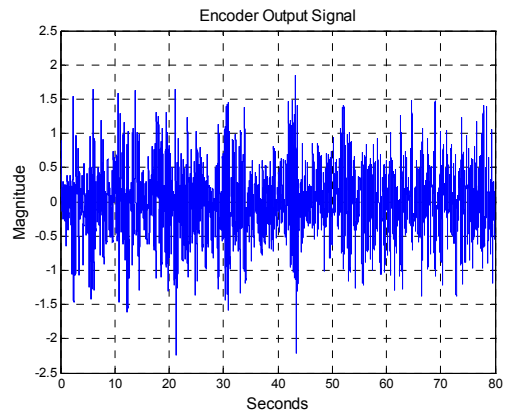


Figure 52. Encoder output

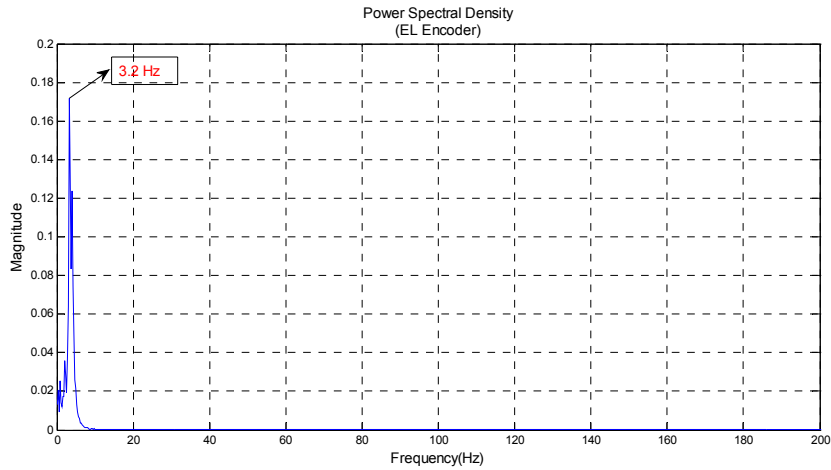


Figure 53. PSD 1

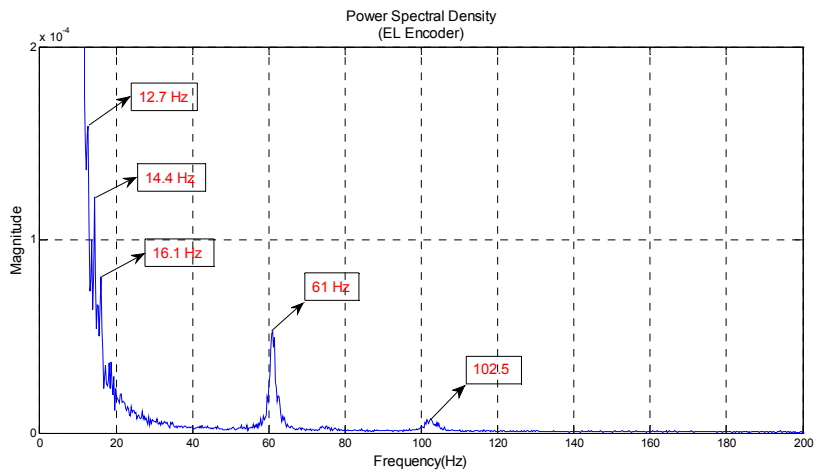


Figure 54. PSD 2

3.1.1.3. Summary and discussion

A number of resonances were measured in the wide band of test frequency range and are summarized in Table 6. The lowest frequency of EL axis is higher than that of AZ since the EL gimbal mechanism is smaller, rigid, and simpler. The gyro shows many more resonance frequencies than the encoder, since it detects angular velocity while the encoder measures angular position.

Table 6. Summary of resonance frequency

Direction	Output signal	Resonance frequencies (Hz)
AZ	Gyro	2.6, 8.3, 11.4, 15.9, 36.6, 69.5, 101, 134, 147.7
	Encoder	2.6, 8.2, 11.4, 101
EL	Gyro	3.8, 10, 14.9, 43.3, 61.4, 74.5, 101, 145, 195
	Encoder	3.8, 11.6, 61.4, 101

3.1.2. Rate loop servo bandwidth

In order to measure the bandwidth of the rate loop, a sweep sine signal was applied to the rate command and output signal was taken from the gyro. Test scheme and data analysis flow are shown in Figures 55 and 56.

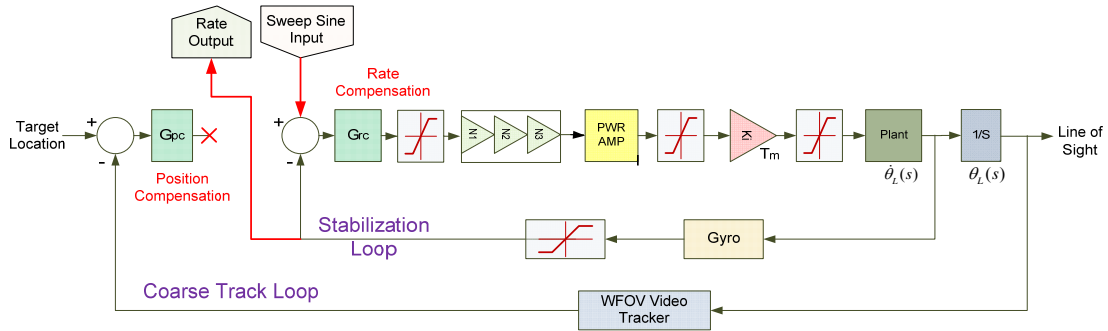


Figure 55. Test point of servo bandwidth

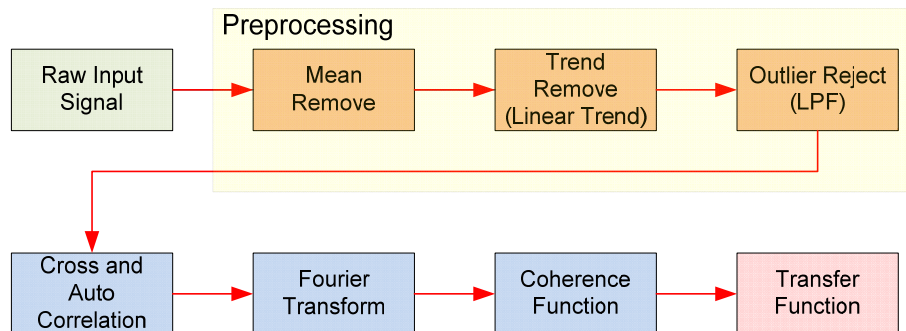


Figure 56. Bandwidth analysis flow

- Correlation analysis

The cross-correlation sequence is defined as

$$R_{xy}(m) = E[x_{n+m} \cdot y_n^*] = E[x_n \cdot y_{n-m}^*]$$

where x_n and y_n are jointly stationary random processes, and $E[\square]$ is the expected value operator. In practice, only a finite segment of one realization of the infinite-length random process is available. Therefore, correlation estimation is calculated as follows:

$$\hat{R}_{xy}(m) = \begin{cases} \sum_{n=0}^{N-m-1} x_{n+m} \cdot y_n^* & m \geq 0 \\ \hat{R}_{yx}^*(-m) & m < 0 \end{cases}$$

The cross-correlation sequence is a length $2 \cdot N - 1$ vector, where x and y are length N vectors ($N > 1$).

- Coherence function

Coherence shows the portion of the output power spectrum related to the input spectrum, according to the following formula:

$$\gamma^2 = \frac{G_{xy} \cdot G_{xy}^*}{G_{xx} \cdot G_{yy}}$$

Where, G_{xy} is the cross spectrum and G_{xy}^* is complex conjugate of G_{xy} , G_{xx} is power spectrum of input and G_{yy} is power spectrum of output.

$$G_{xy} = FFT(\hat{R}_{xy})$$

$$G_{xx} = FFT(\hat{R}_{xx})$$

It is an indication of the statistical validity of a frequency response measurement. Coherence is measured on a scale of 0.0 to 1.0, where 1.0 indicates perfect coherence. Coherence values less than unity are caused by poor resolution, system nonlinearities, extraneous noise and uncorrelated input signals. Because coherence is normalized, it is independent of the shape of the frequency response function.

- Transfer function

Frequency response, often called the “Transfer function” is calculated as the ratio of the cross spectrum to the input power spectrum.

$$H(f) = \frac{G_{xy}}{G_{xx}}$$

3.1.2.1. Test scenario

Sweep sine signals were applied to the rate command input with peak input voltage of 0.02V for EL axis, and 0.05V for AZ axis. Sweep frequency was 1 Hz to 50Hz and output signals were taken from the respective gyro. Test schemes are shown in Table 7.

Table 7. Scenario for servo bandwidth test

Direction	Input (Vpk)	Input Type	Measured Data Analysis	
			Freq. Range (Hz)	Output Position
EL	0.02	Sweep sine	1-50	EL Gyro
AZ	0.05	Sweep sine	1-50	AZ Gyro

3.1.2.2. Test results

For each axis, excitation and output signals are plotted in the time domain and magnitude plots of frequency response are shown in the figures below.

- AZ axis

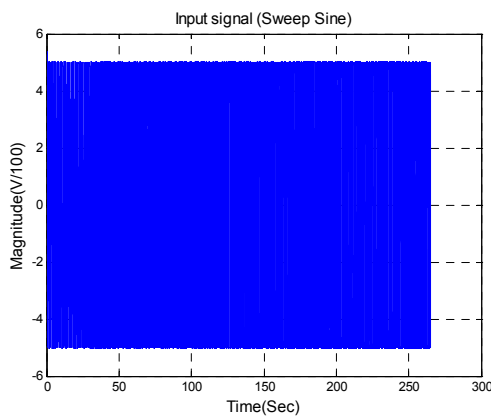


Figure 57. Rate input

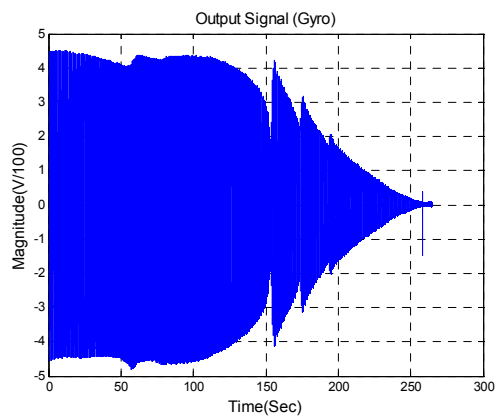


Figure 58. Gyro output

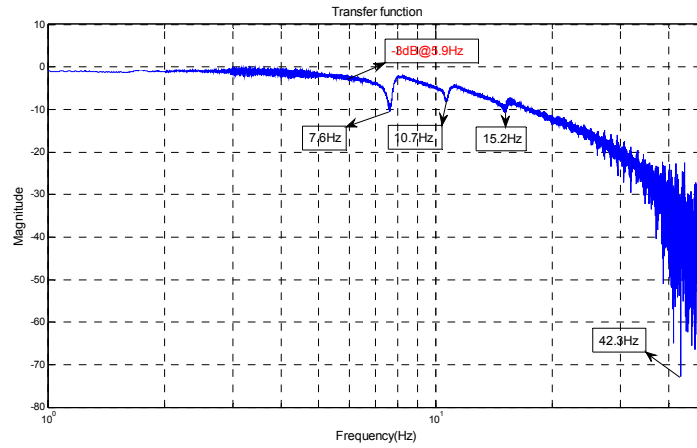


Figure 59. AZ transfer function

- EL axis

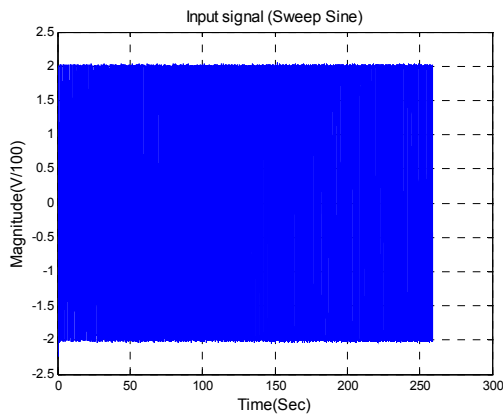


Figure 60. Rate input

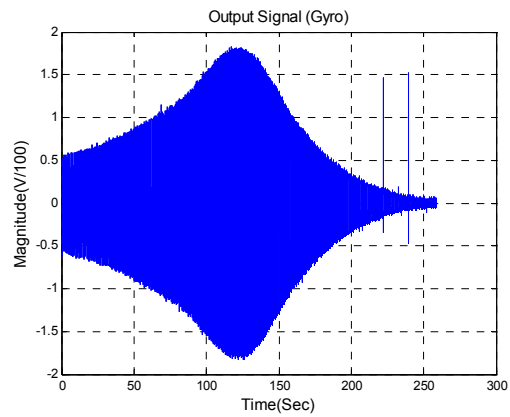


Figure 61. Gyro output

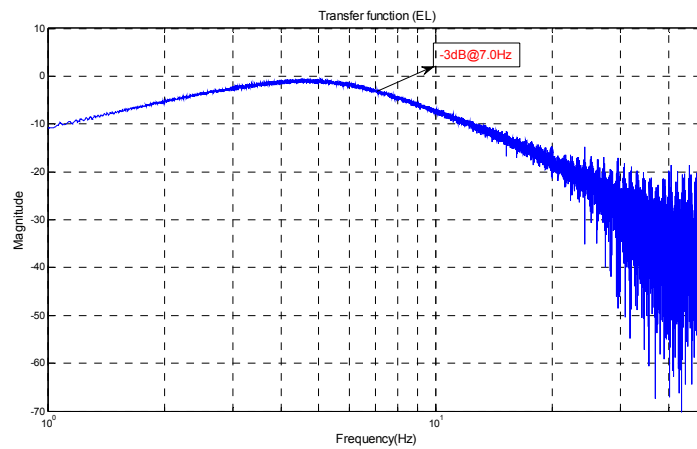


Figure 62. EL transfer function

3.1.2.3. Summary and discussion

The test results shows there are large steady state errors for both axis and -3dB bandwidth is 6Hz for AZ axis, and 7Hz for EL axis. It is also shown that the resonance frequencies of AZ axis at 8.2Hz, 11.4Hz, 15.9Hz cause degradation of tracking performance.

3.1.3. Rate loop stabilization

Torque rejection characteristics were determined by applying a disturbance input to the power amplifier measuring torque error. A Sweep sine signal was used as the input signal with a frequency range of 1-100Hz. Test scheme and scenario are shown in Figure 63 and Table 8.

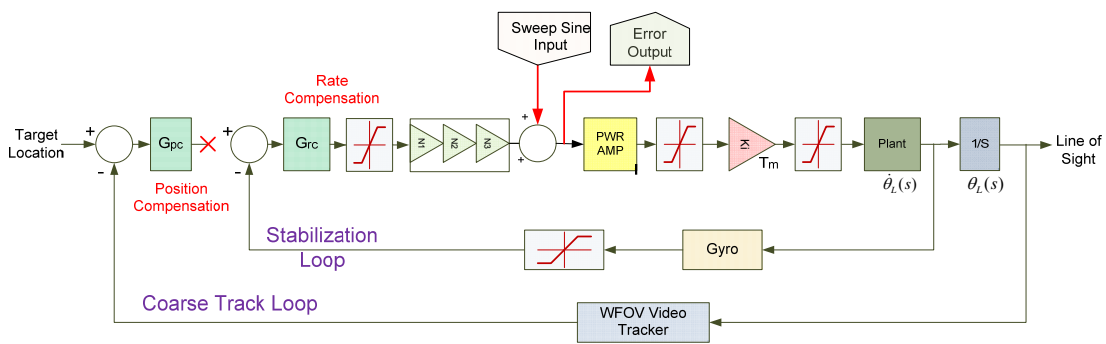


Figure 63. Test point of resonance

Table 8. Scenario for stabilization test

Dir.	Input Voltage (Vpk)	Torque Disturbance Input Type	Measured Data Analysis	
			Freq. Range (Hz)	Output Position
EL	0.5	Sweep sine	1-100	EL Error
AZ	0.5	Sweep sine	1-100	AZ Error

3.1.3.1. Test results

Excitation input and error output are plotted in the time domain and frequency response of the output signal are shown in the figures.

- AZ axis

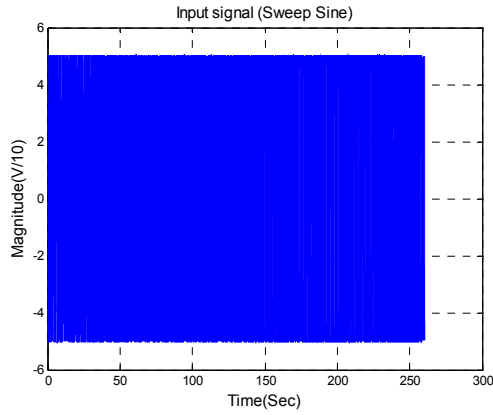


Figure 64. Disturbance input

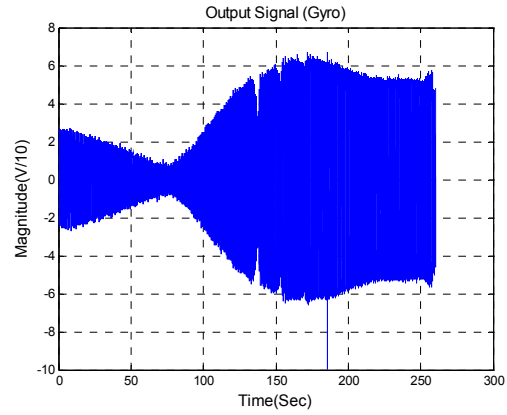


Figure 65. Error output

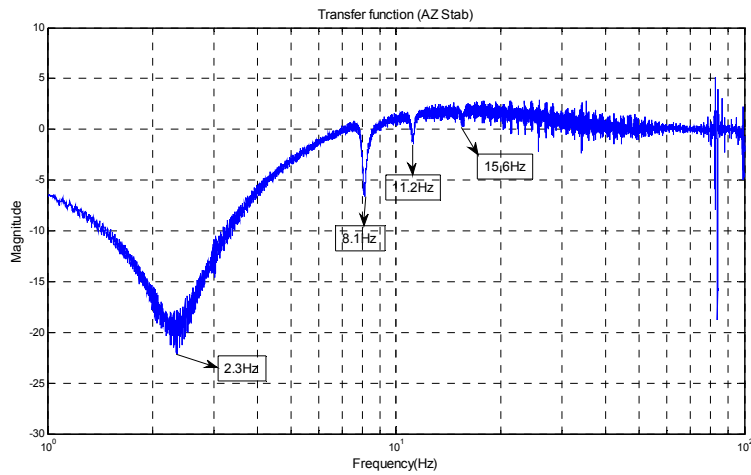


Figure 66. AZ transfer function

- EL axis

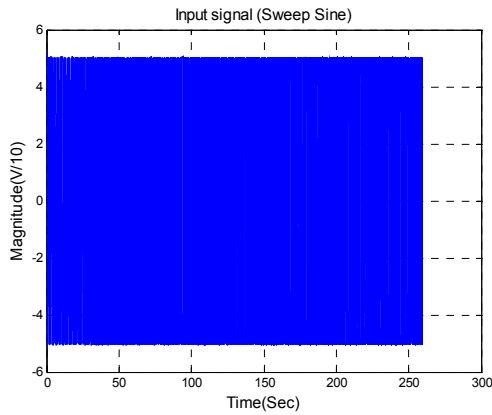


Figure 67. Disturbance input

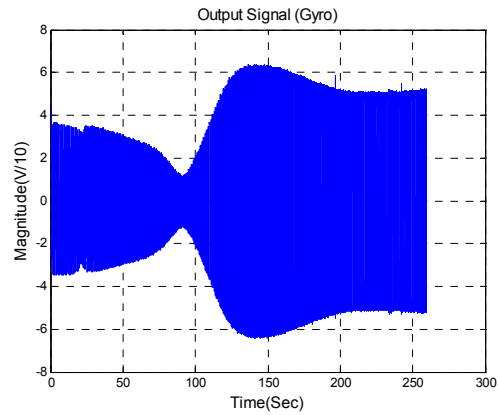


Figure 68. Error output

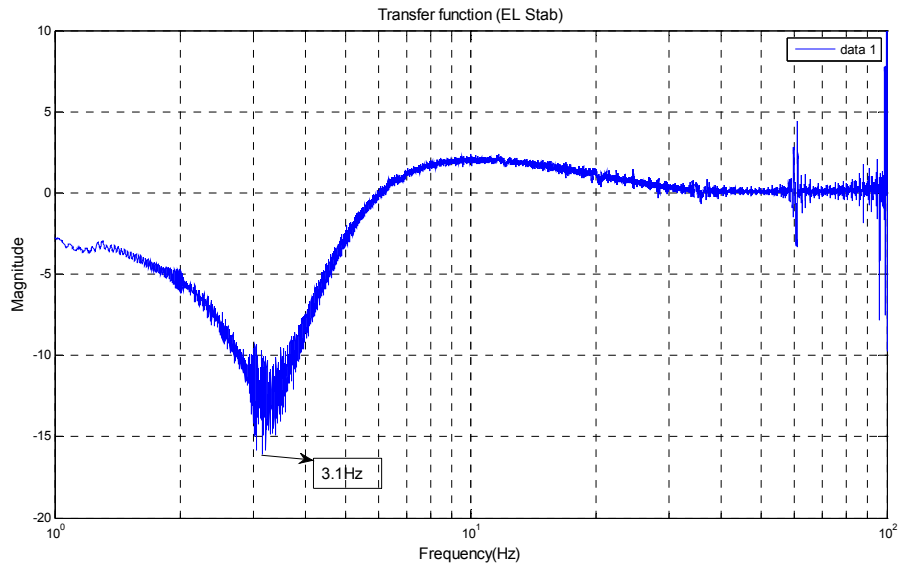


Figure 69. EL transfer function

3.1.3.2. Summary and discussion

The transfer function shows that torque rejection ratio is low in the test frequency range. Additionally, resonance frequencies affect the stabilization performance as well as servo tracking.

3.2. NFOV control loop

3.2.1. Fast steering mirror

FSMs have been used for several years in military and aerospace applications for target acquisition, scanning, and beam steering. Two axis mirrors are driven by a push/pull configuration voice coil. It is similar to speaker coil, however unlike a speaker, the FSM is configured with a moving magnet instead of a moving coil. The mirror is flexurally suspended and has a built in optical sensor and is configured as locally feedback system. Local position feedback is the inner loop of the NOFV control loop. In order to get the dynamic characteristics of the FSM, a sweep sine was applied to the local position input command and output was taken from the position sensor as shown in Figure 70.

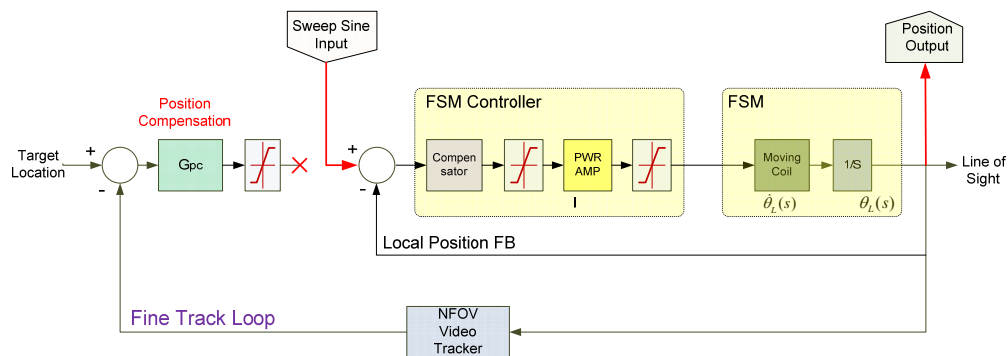


Figure 70. Test point of FSM

Magnitude of input sweep sine was 0.5V and frequency measurement range was 1-1000Hz. Test schemes are summarized in Table 9.

Table 9. Scenario for FSM test

Dir.	Voltage Magnitude of Input (Vpk)	Input Type	Measured Data Analysis	
			Freq. Range (Hz)	Output
X	0.5	Sweep sine	1-1000	x-Position
Y	0.5	Sweep sine	1-1000	y-Position

Frequency response test results are shown in Figures 71 and 72. The transfer function of each axis is nearly identical and both have a -3dB bandwidth of 360Hz.

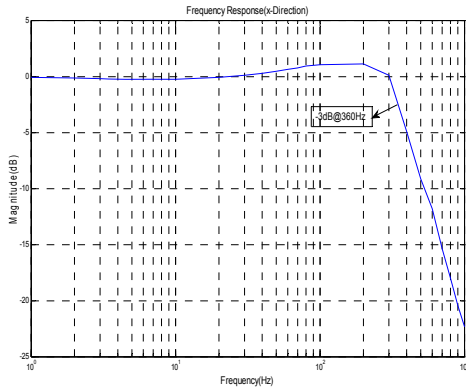


Figure 71. AZ transfer function

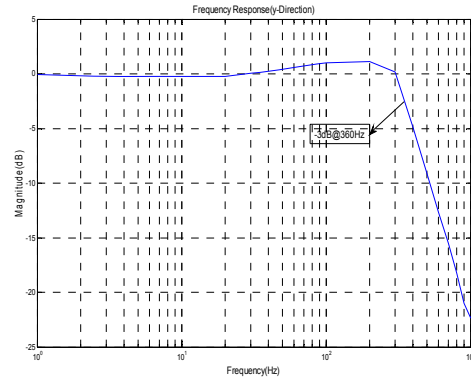


Figure 72. EL transfer function

3.2.2. NFOV bandwidth

One scheme for frequency response testing of the NFOV video tracker is shown in Figure 73.

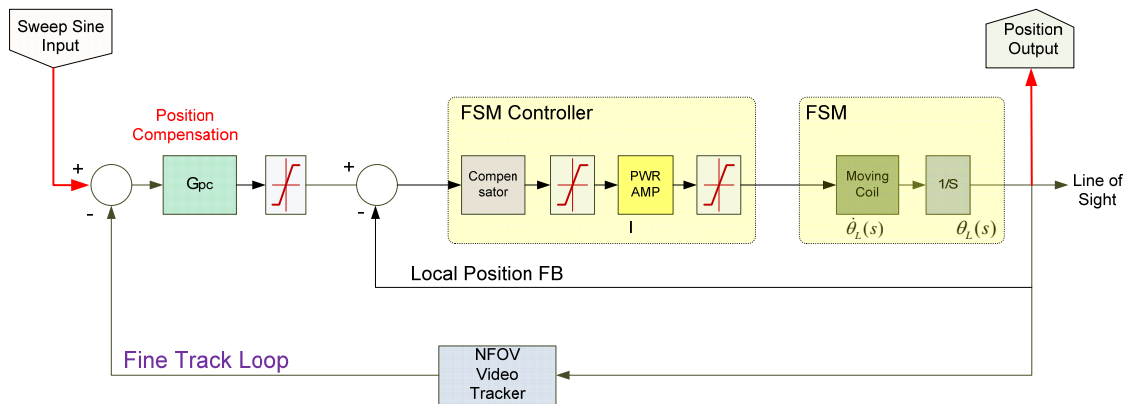


Figure 73. Test point of NFOV track loop

In real environments though, frequency response testing of the video tracker is not easy because there are numerous difficulties in generating sweep sine target motion, and furthermore, the system does not provide position values of the target. Instead of a test method similar to Figure 73, an alternative scheme using two FSMs is applied for the bandwidth test as shown in Figure 74. A Sweep sine signal is applied to the position input of the FSM and the output signal is measured as the position output of the second FSM.

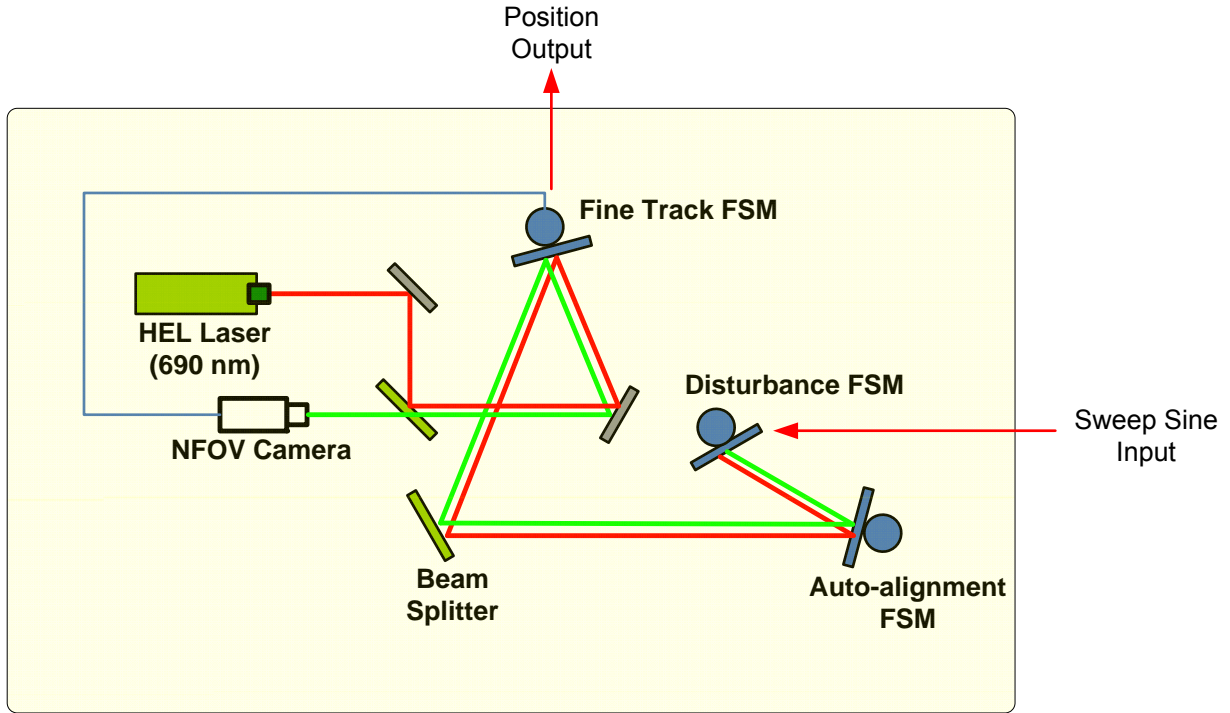


Figure 74. Test scheme of NFOV track loop

Magnitudes of the test signals were 0.5V, and 1.0V while sweeping range of the frequency was 0.1-100Hz, as shown in Table 10.

Table 10. Scenario for NFOV track loop test

No.	Dir.	Input (Sweep sine)			Fine Track FSM Output Pin
		Disturbance FSM Input Pin	Sweep sine Magnitude	Frequency	
1	X (AZ)	x+ (4)	0.5V(=1.31mil)	0.1~100 Hz	x-Pos (pin 14) GND(22,16)
2		x- (3)	1.0V(=2.62mil)	0.1~100 Hz	
3	Y (EL)	y+ (13)	0.5V(=1.31mil)	0.1~100 Hz	y-Pos (23) GND(22,16)
4		y- (12)	1.0V(=2.62mil)	0.1~100 Hz	

Regardless of input magnitude, transfer function for each axis was almost the same and -3dB frequency was measured as 13Hz. The results are shown in Figures 75-76.

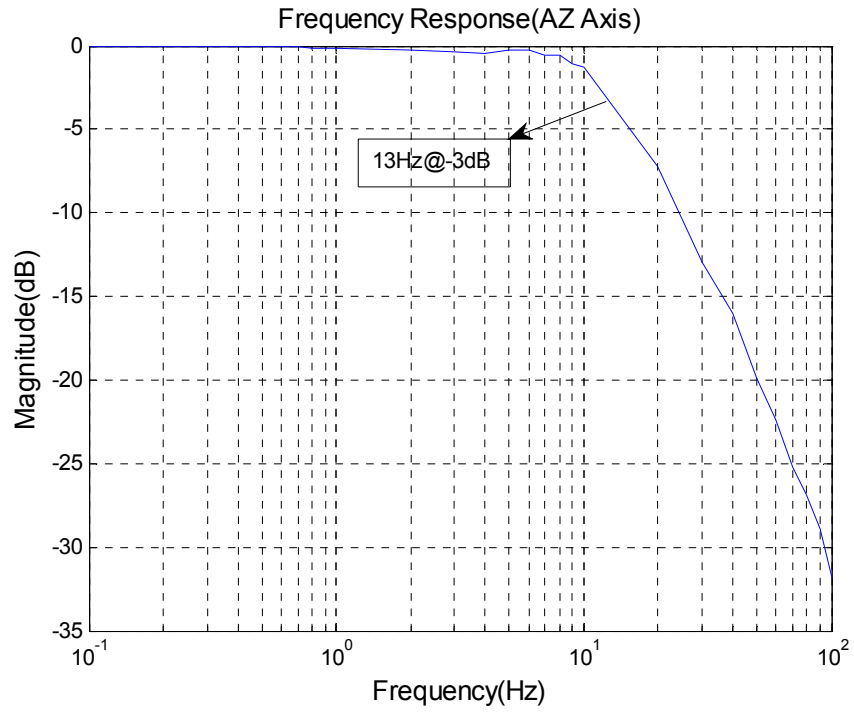


Figure 75. AZ transfer function

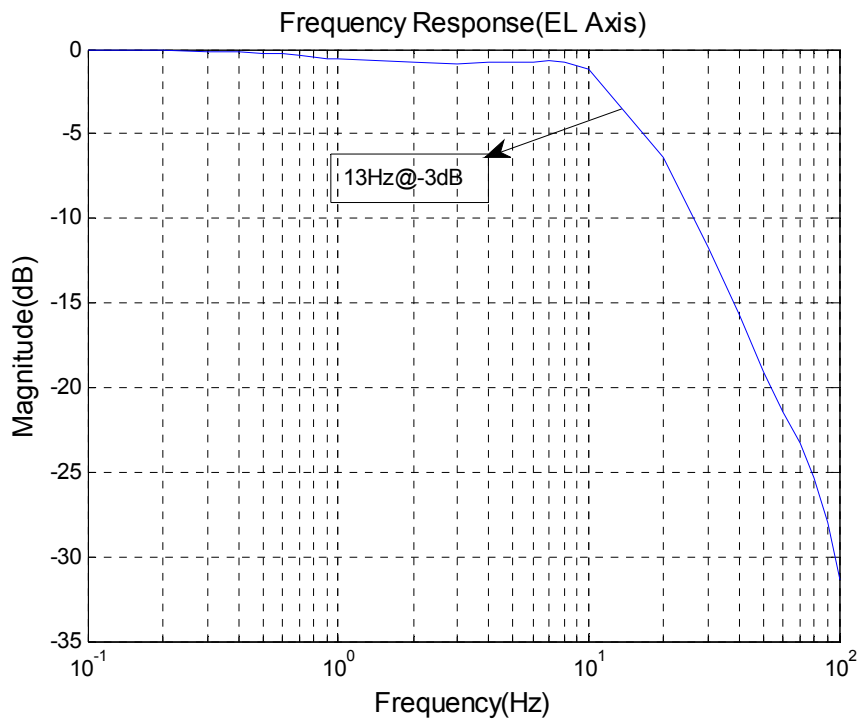


Figure 76. EL transfer function

4. MODELING AND SIMULATION

Mathematical model is important to estimate system performance and to design new control algorithms for performance improvements. Some mathematical models of subsystem were found through experiments, others were from the specifications of the components. Models for servo components such as gyro, power amplifier are made from the respective data sheets. Based on the component models and experimental results, local control loop and whole integrated models were built using Matlab Simulink.

4.1. Component modeling

4.1.1. Gyro

The gyro measures angular rate of rotation, which can be integrated to allow turning angle to be measured accurately. The DSP-3000 that is mounted on the 2 axis gimbal, is a single axis fiber optic gyro outputting a digital signal. The gyro provides high speed TTL(Transistor-to-Transistor Level) synchronous serial interface with a standard output rate of 1000/sec.

- General

- Manufacturer : KVH Industries

- Model : DSP-3000

- Part Number : 02-1222-02 Digital, 1000Hz synchronous

- Specifications

Attribute	Rating	Remark
Maximum Input Rate	$\pm 375^\circ/\text{sec}$	
Scale Factor		
-Linearity(room temp)	-1000 ppm, 1σ of full scale for $\pm 375^\circ/\text{sec}$	1 LSB = $60\mu^\circ/\text{s}$
	-500 ppm, 1σ of full scale for $\pm 150^\circ/\text{sec}$	
-Temperature Sensitivity	-500 ppm, 1σ	
-Error(full rate & temp)	-1500 ppm, 1σ	

Bias -Offset(room temp) -Stability(room temp) -Temperature Sensitivity	±20°/hr 1°/hr, 1σ 6°/hr, 1σ	
Bandwidth(3 dB)	> 400Hz	
Update Rate	1000/sec	
Angle Random Walk(noise)	4°/hr/√Hz 0.0667/√hr	
Initialization Time	< 5 sec	
Electrical -Input Voltage -Power consumption	+5Vdc ± 10% 3 watts Max.	
Output -Type -Format(selectable)	3.072 MHz serial, Rate, Incremental Angle, Integrated Angle	
Physical -Dimensions -Weight	3.5" * 2.3" * 1.3" 0.6 lbs (270 g)	
Environmental -Operating Temperature -Storage Temperature -Shock(Functional) -Random Vibration -MTBF	-40°C to +75°C -50°C to +85°C Functional Sawtooth 40g, 6-10ms 20 to 2000Hz, 8g rms, Operational > 55,000 hr, ground mobile	

One of the important items for a dynamic control system is bandwidth. Since the -3dB bandwidth is greater than 400Hz, a mathematical model of the gyro is expressed as follows:

$$G_{Power-AMP} = \frac{w_n^2}{s^2 + 2\xi w_n s + w_n^2}, w_n = 2 * \pi * f, f = 400, \xi = 0.707$$

4.1.2. Power amplifier

The amplifier has a jumper selectable operating mode including velocity command mode, torque(current) command mode, dual phase command mode, and

differential dual phase command mode. In the HEL testbed, dual phase command mode is used. The dual phase inputs are sinusoidal and are 120° out of phase from each other. The third phase is internally generated by the amplifier. The advantage of this configuration is that it provides the smoothest possible motion and also minimizes motor torque ripple for maximum accuracy. Major characteristics of the power amplifier are summarized as following:

- General
 - Manufacturer : Aerotech Inc.
 - Model : BL10-80-A
 - Amplifier option : CM1-PK100-CC50
- Specifications

Attribute	Rating	Unit
Output		
-Power Amp Voltage	160	Vdc
-Command Voltage	±10	Vdc
-Peak Output Current	10 (Sustain for 1 sec, Load dependent)	A
-Continuous Output Current	5 (Continuous sinewave, Load dependent)	A
-Peak Output Power	1,350	Watts
-Continuous Output Power	675	Watts
Input		
-Voltage	115 single phase	Vac
-Current	10 A Max.	A
Power Amp Gain	1	A/V
Power Amp Bandwidth	2 (Into a BLM-203-A, 4Ohm/3.2mH)	KHz
Minimum Load Resistance	0.5	Ohms
Weight	8.5	Kg

Options -CM1 -PK100 -CC50	-Brushless Motor, 0° Commutation Offset -Peak Current Output 100% of max -Continuous Current output before automatic shutdown 50% of max	
------------------------------------	--	--

According to the above specification, mathematical model of amplifier can be thought of as a LPF which has -3dB bandwidth of 2KHz and is expressed as follows:

$$G_{Power-AMP} = \frac{w_n^2}{s^2 + 2\xi w_n s + w_n^2}, w_n = 2 * \pi * f, f = 2000, \xi = 0.707$$

4.1.3. Fast steering mirror

The fast steering mirror consists of a one inch glass with a user replaceable mirror/sub-mount where the mirror is hard mounted to the mirror gimbal. A built-in high precision optical sensor monitors mirror angles. The compact optical head is attached to a servo controller using a supplied 6 foot cable. The user inputs analog mirror commands to the controller which steers the mirror.

- General

- Manufacturer : Optics in Motion.

- Model : OIM 101

- Specifications

Attribute	Rating	Unit
Dynamic performance		
-Mirror angle range	+/- 1.5	Degrees
-Angular resolution	< 2	uRads
-3 dB bandwidth	>850	Hz
-Linearity	1 %	% FS
-Step response	< 5	ms
Mirror substrate		
-Material	Pyrex	
-Mirror substrate size	1" * 0.25"	
-Coating	Protected Aluminum	

Electrical -Peak power	30	Watts
Mechanical -Mirror head size -Controller size	2.3 * 2.3 * 2.2 2.0 * 4.0 * 6.1	Inches Inches

The position sensor provides mirror feedback information to the controller which can also be monitored by the user. The local position sensor outputs a voltage which is proportional to the mirror angular position. The position sensor scale factor is 10Volts = 1.5 Degrees and has a range from +10Volts to -10Volts. The frequency response tests in the previous section showed that the -3dB bandwidth of the locally closed position loop is 360Hz. Therefore, the FSM can be regarded as a 2nd order LPF and expressed as

$$G_{FSM} = \frac{w_n^2}{s^2 + 2\xi w_n s + w_n^2}, w_n = 2 * \pi * f, f = 360, \xi = 0.707$$

4.1.4. ALAR

The ALAR which is direct drive rotary stage, provides superior angular positioning and velocity control with large aperture. With the combination of a large aperture and direct drive motor, the rotary stage has no backlash, and no gears or gear vibrations. Applications of the ALAR include single and multi-axis electro optical sensor testing, missile seeker testing, antenna testing, inertial navigation device testing, photonic component alignment, and high accuracy laser testing.

- General

- Manufacturer : Aerotech Inc.

- Model : ALAR-100-SP-ES16286

- Incorporate BLDC Motor and High performance Rotary Encoder

- Specifications

Attribute		Rating	Unit
Motor	-Model	S-180-44-A	
	-Continuous Current		
	.Apk	2.7	A
	.Arms	1.9	A
	-Peak Current	10.7	A
	-Torque Constants		
	.Continuous	2.77	N-m/A
	.Peak	3.92	N-m/A
	-Peak Torque	30.0	N-m
	-Number of poles	18	
	-Cold Resistance	12.8	Ohms
-Inductance	3.4	mH	
-Rotor Inertia	0.0074	Kg-m ²	
Encoder	-Resolution	199.6	uRad
ALAR	-Max. Limited Travel	±170	Deg
	-Max. Velocity	300	RPM
	-Max. Acceleration	1364	Rad/s ²
	-Max. Torque	23.9	N-m
	-Continuous Torque	6.0	N-m
	-Shaft Inertial	0.022	Kg-m ²
	-Position Accuracy		
	.Repeatability	±2.4 (0.5 arc-sec)	uRad
.Accuracy	±18.9 (3.9 arc-sec)	uRad	
.Wobble	9.7 (2.0 arc-sec)	uRad	

4.1.5. Limit

The HEL testbed is a digital/analog mixed electro-mechanical control system which has several limit sources: voltage limit due to the electronic devices and current/torque/angular velocity limits due to the servo components such as power amplifier, ALAR, and gyro. Limit function and items are described in Figure 77 and Table 11.

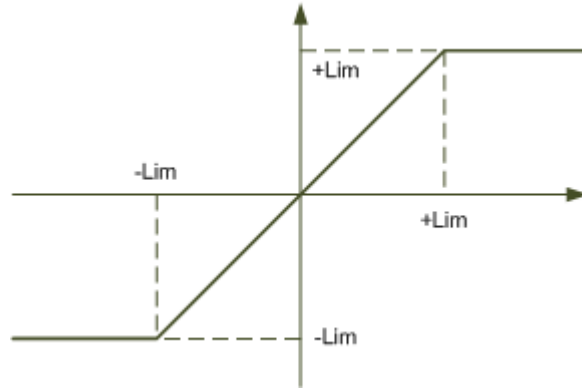


Figure 77. Limit function

Table 11. Summary of limit function

Items	Limit value	Unit
Voltage Limit	±10	Vdc
Current Limit	±10	A
Torque Limit	±23.9	N-m
Gyro Limit	±375	°/sec

4.1.6. Disturbance model

A disturbance input model used in HEL testbed model which came from a ground fighting vehicle is expressed as following a power spectral density function. RMS value of the disturbance is 83mil/sec.

$$PSD = \frac{31.2 * 10^3 f}{(1 + 4f^2)^{3/2}} \cdot \frac{(mil / sec)^2}{Hz}, 0.25 \leq f \leq 50Hz$$

4.2. WFOV control loop

According to the mathematical model, the WFOV control loop which consists of inner loop and outer loop, is constructed as shown in Figure 78. The Inner loop, using gyro feedback, is a rate control loop that provides stabilization function with respect to external disturbances and tracking functions. The Outer loop, based on the WFOV

camera feedback, is an angular position control loop that automatically maintains LOS to the center of the target.

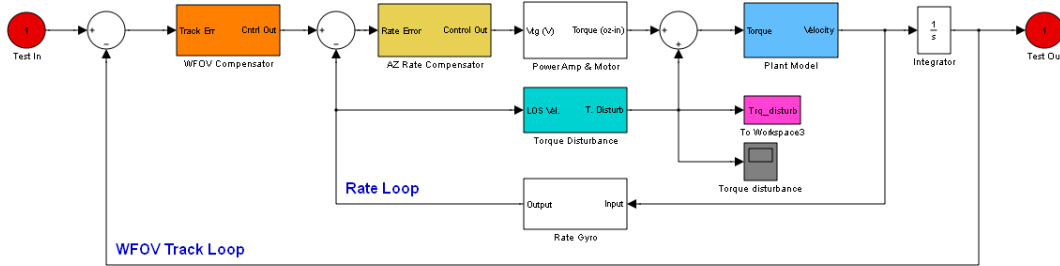


Figure 78. WFOV Simulink model

4.2.1. Rate control loop

Simulation results of each axis for the step response and corresponding transfer function are shown in Figures 79-82. The bandwidth of the control model is the same as that of experiment results. However, the shape of the response at low frequencies and around the mechanical resonant frequency is a little different from the experiment results. The reason is that gimbal was assumed to be a simple linear model in the simulation and account for any resonance or nonlinear effects.

- AZ axis

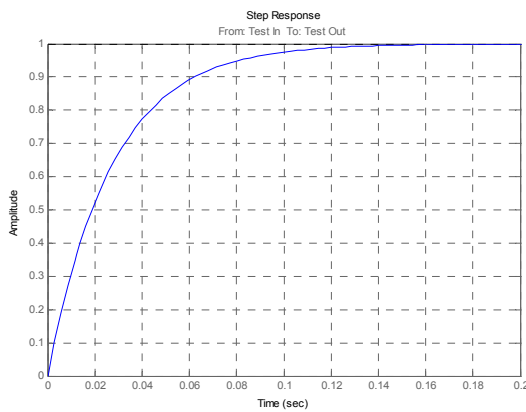


Figure 79. AZ step response

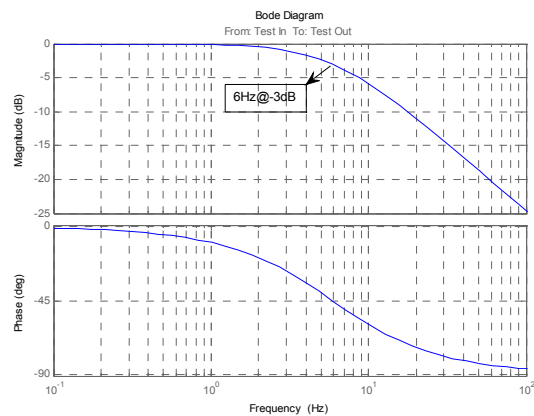


Figure 80. AZ transfer function

- EL axis

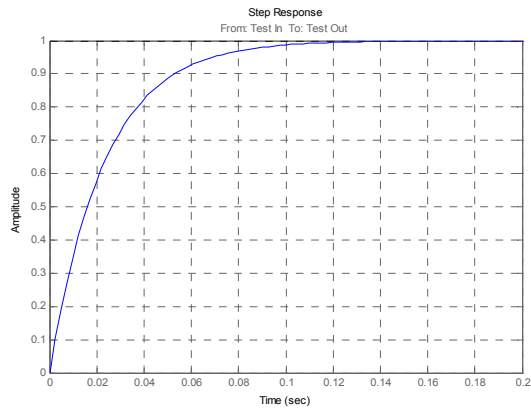


Figure 81. EL step response

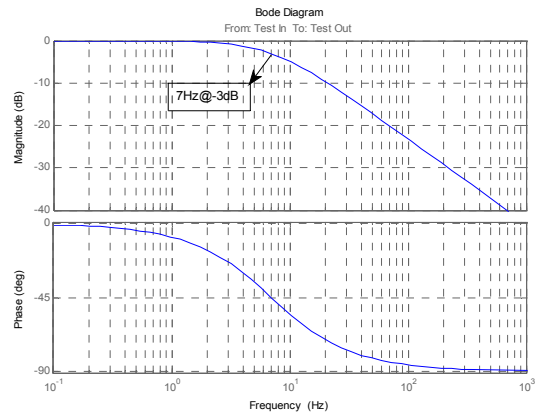


Figure 82. EL transfer function

4.2.2. Position control loop

Test results of outer position loop are shown in Figures 83-86. Parameters used in the model and test results are summarized in Table 12.

- AZ axis

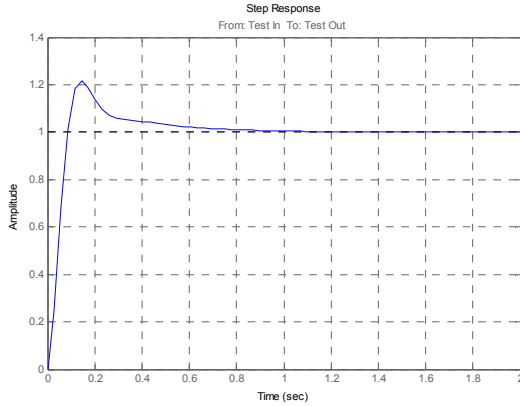


Figure 83. AZ step response

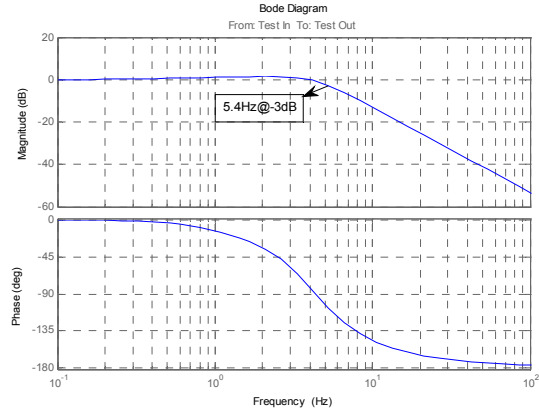


Figure 84. AZ transfer function

- EL axis

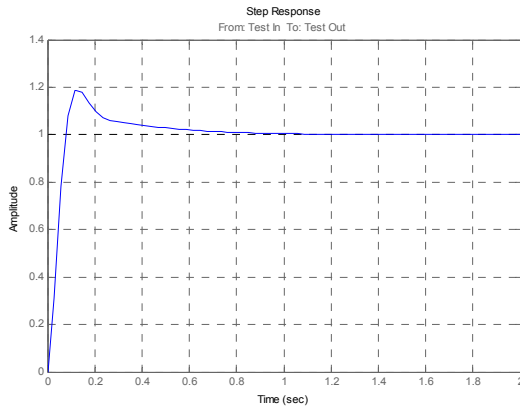


Figure 85. EL step response

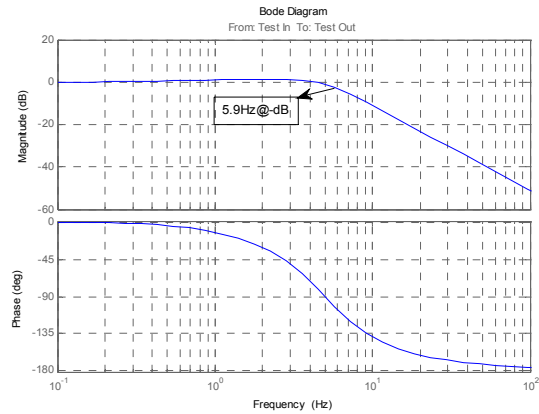


Figure 86. EL transfer function

Table 12. Summary of WFOV parameters

Items		AZ axis	EL axis
Gimbal Inertia		1000 in-oz	260 in-oz
Rate loop	Compensator	94.4 (P-controller)	28.8 (P-controller)
	-3dB BW	6Hz	7Hz
WFOV position	Compensator (PI-controller)	$\frac{0.0063s + 0.01982}{s}$	$\frac{0.006918s + 0.02173}{s}$

loop	-3dB BW	5.4Hz	5.9Hz
------	---------	-------	-------

4.3. NFOV control loop

The control model of the NFOV control loop is shown in Figure 87. The model consists of a fast steering mirror which is a 2nd order system as shown in the previous experiment results along with a compensator. The compensator is a simple integrator type and summarized in Table 13 for each axis. Test results of the step response and frequency response for one axis are shown in Figures 88-89 since each axe of NOV has identical characteristics. Bandwidth of the model is also the same as that of experiment results.

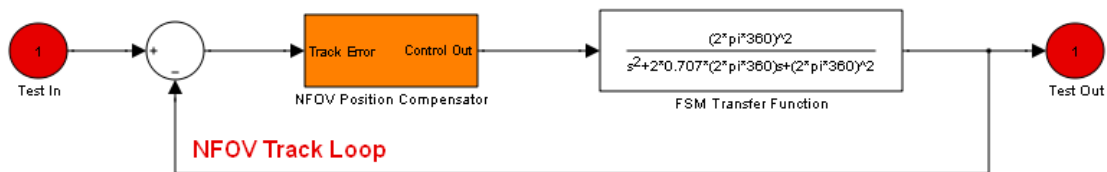


Figure 87. NFOV Simulink model

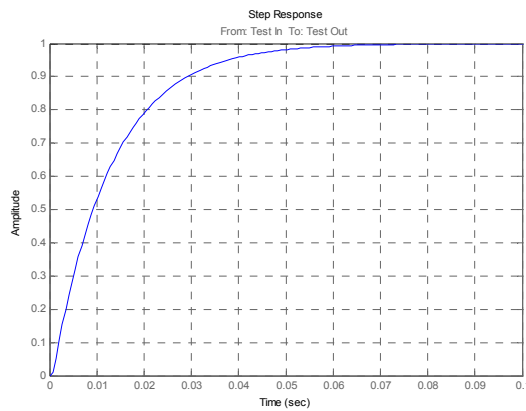


Figure 88. Step response

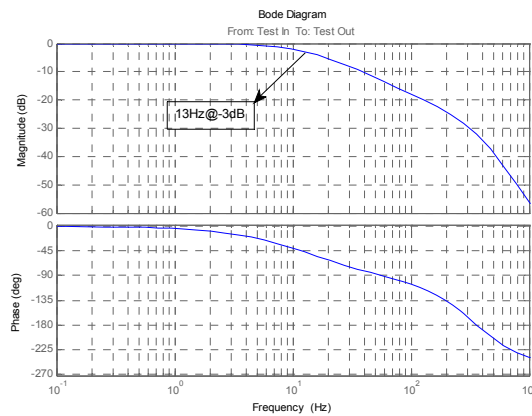


Figure 89. Frequency response

Table 13. Summary of NFOV parameters

Items	AZ axis	EL axis
Compensator (I-controller)	$\frac{1.2388}{s}$	$\frac{1.2388}{s}$
-3dB BW	13Hz	13Hz

4.4. Integrated control model

An integrated model of the HEL testbed, which consists of WFOV and NFOV track loops, is shown in Figure 90. The lower part of the model is the WFOV block that has an inner rate control loop and an outer position control loop. Upper portion shows the NFOV track loop.

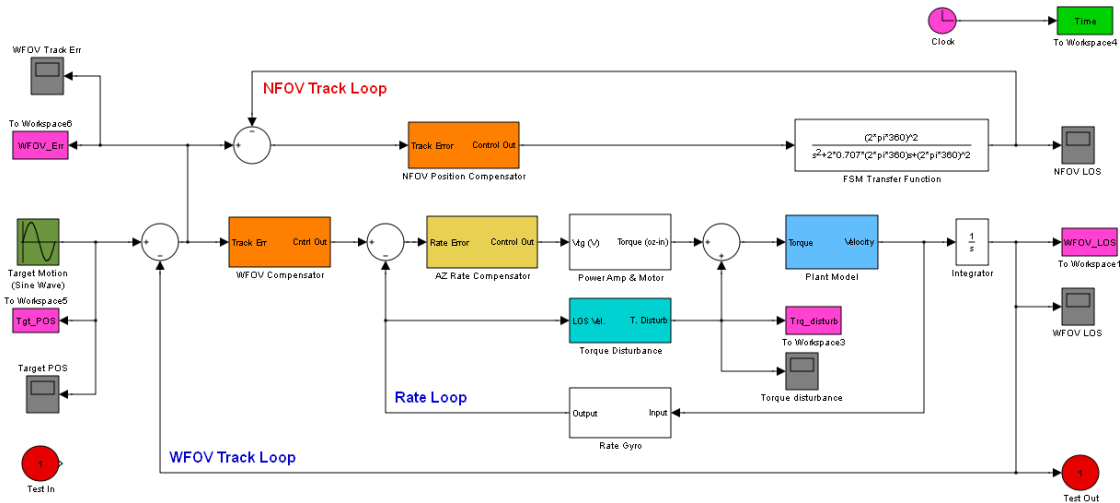


Figure 90. Integrated HEL model

Test results for the integrated model are shown in Figures 91-98. Two kinds of performances were investigated in the tests.

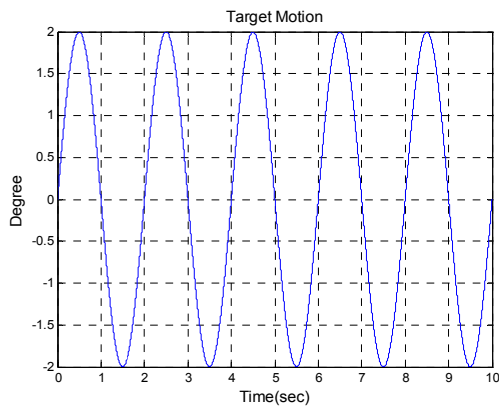


Figure 91. Target motion

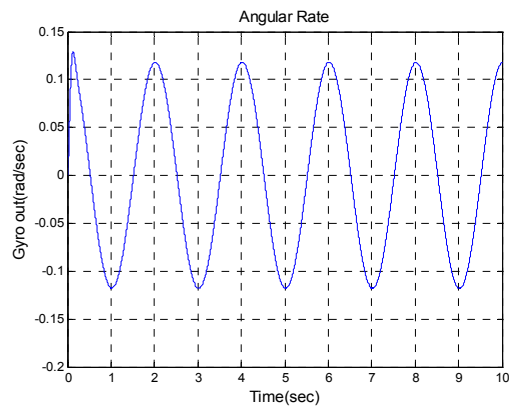


Figure 92. Rate of WFOV LOS

The first test is on the target tracking performance as shown in Figures 91-94. Test input signal of the target motion is sinusoidal with 2 degree peak and frequency of 0.5Hz. In the steady state, peak tracking error of the WFOV tracker is around 2.5 mrad and error of the NOFV is decreased to less than 0.1 mrad.

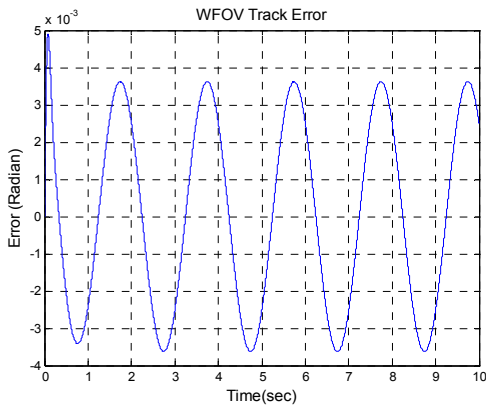


Figure 93. WFOV track error

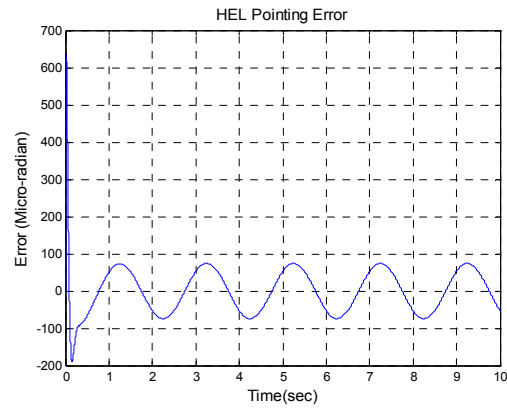


Figure 94. NFOV track error

The second test is on the disturbance rejection characteristics as shown in Figures 95-98. The disturbance input was a band limited random signal with 83mil/sec rms, which is described in the previous section, and shown in Figure 95. Peak error of the WFOV track loop was approximately 40 mrad and error of the NFOV is less than 10 mrad, as shown in Figures 97-98.

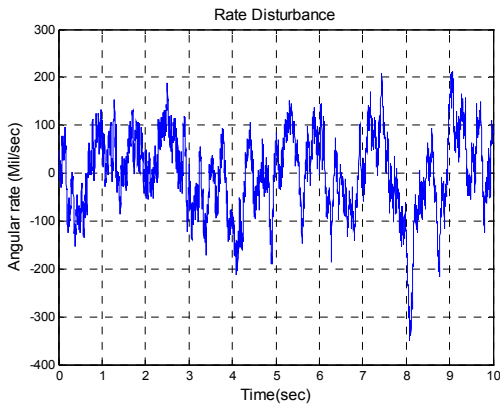


Figure 95. Disturbance input

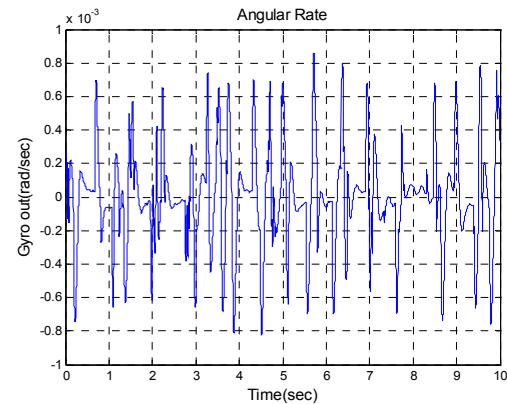


Figure 96. Rate of WFOV LOS

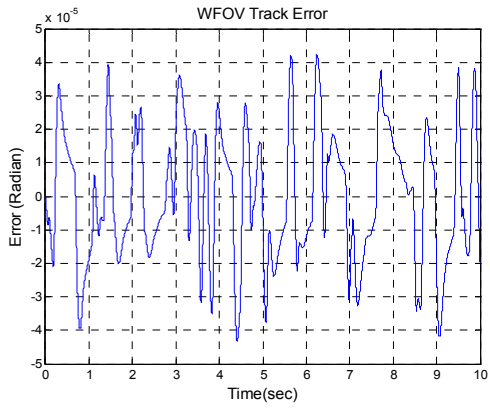


Figure 97. WFOV track error

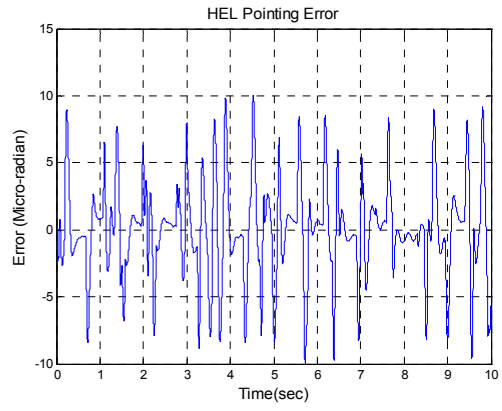


Figure 98. NFOV track error

5. COMPENSATOR DESIGN

Undesired fluctuations in the pointing of a laser beam reduce the accuracy of the beam pointing at the target due to a target motion and external disturbances. The accurate pointing of laser beam is necessary for the application of laser communication and defense systems. For example 100 mrad of jitter at 10Km will result in 1m movement of the beam center. Furthermore, disturbance characteristics often change with time and environment, therefore optimal performance of a beam steering system requires an adaptive control system.

5.1. Feed forward control

In some cases, the major input to a process may be measured and utilized to provide feed forward control. The advantage of feed forward control is that corrective action is taken for a change in input before it affects the control parameter. Feed forward control is used in conjunction with feedback control to provide multiple input single output control. In the HEL integrated control model, WFOV track error is taken and applied to the control input of the NFOV track loop. Test results for the feed forward control are shown in Figures 99-102. Peak of the NFOV track error for the target motion input is reduced from 80 mrad to 0.3 mrad and error with an external disturbance present is reduced from 10 mrad to 0.025 mrad.

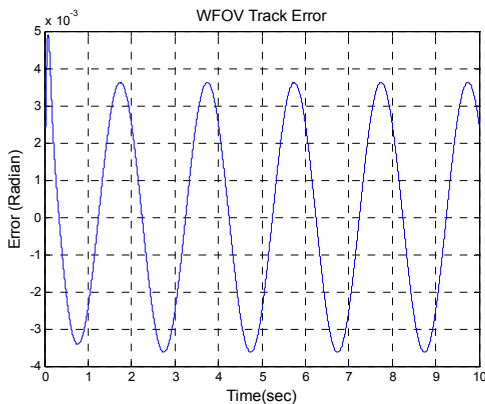


Figure 99. WFOV track error

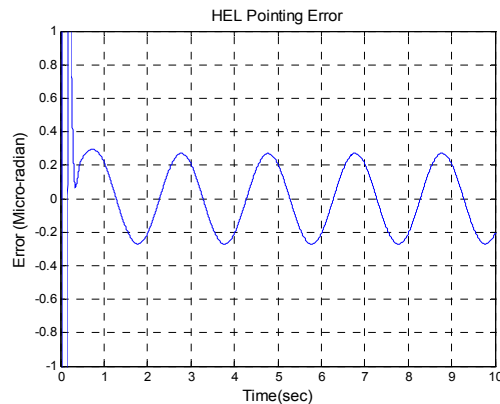


Figure 100. NFOV track error

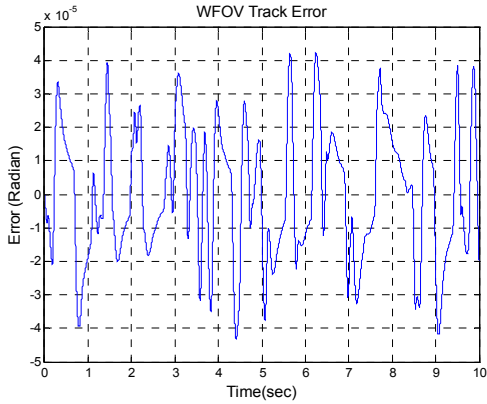


Figure 101. WFOV track error

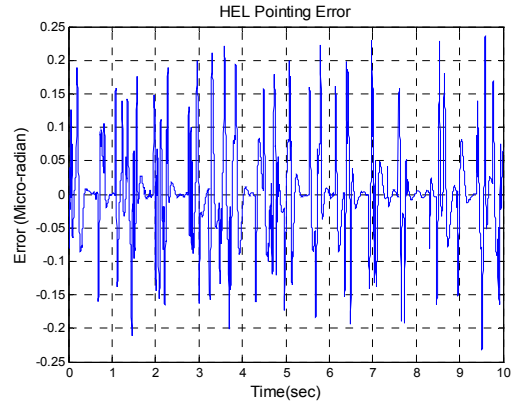


Figure 102. NFOV track error

5.2. Adaptive filter with F/F control

LMS (Least Mean Square) is a linear adaptive filtering algorithm and has been successfully used in signal processing applications. A significant feature of the LMS algorithm is its simplicity as it does not require measurement of correlation functions, nor does it require matrix inversion. In reality, it is not easy to find the correlation matrix of input and the cross correlation vector between input and desired response. The algorithm consists of two basic processes: a filtering process and an adaptive process. The combination of these two processes working together constitutes a feedback loop as illustrated in the block diagram of Figure 103.

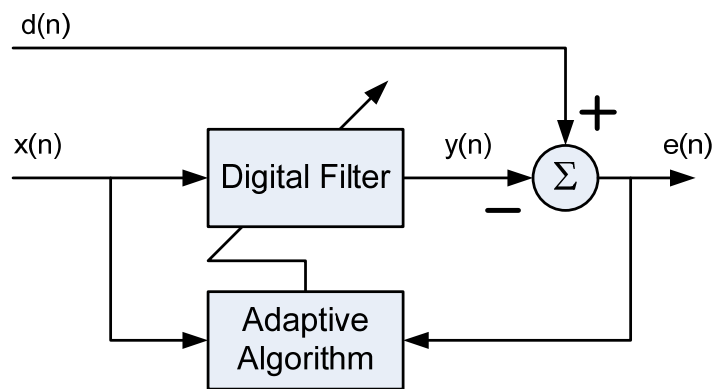


Figure 103. Block diagram of adaptive filter

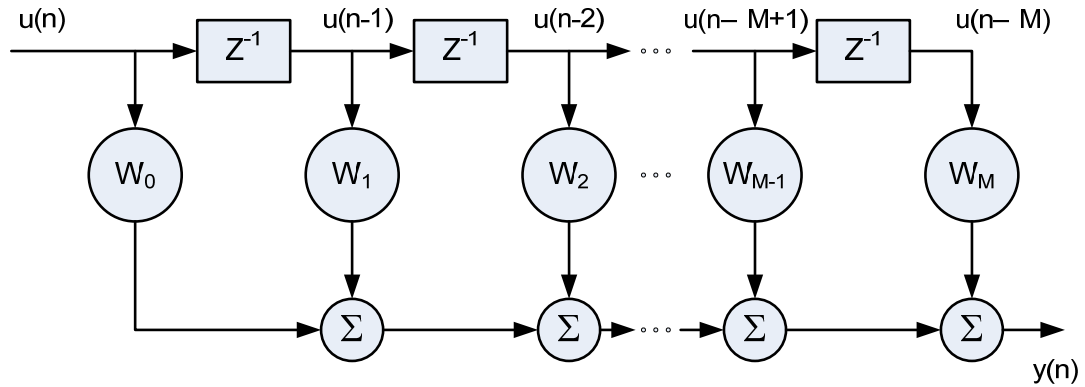


Figure 104. Detailed structure of the filter component.

The tap inputs $u(n), u(n-1), \dots, u(n-M)$ form the elements of the $(M+1)$ -by-1 tap input vector $\mathbf{u}(n)$, where M is the number of delay elements. Correspondingly, the tap weights w_0, w_1, \dots, w_M form the elements of the $(M+1)$ -by-1 tap weight vector $\mathbf{w}(n)$. Details of the transversal filter component are presented in Figure 104. The algorithm of the adaptive least mean square (LMS) is described as follows:

- Filter output

$$y(n) = \mathbf{w}^T(n) \mathbf{u}(n) \quad (1)$$

- Estimation error signal

$$e(n) = d(n) - y(n) \quad (2)$$

- Tap weight adaptation

$$w(n+1) = w(n) + \mu \cdot u(n) \cdot e(n) \quad (3)$$

Equations (1) and (2) define the estimation error $e(n)$, the computation of which is based on the current estimate of the tap weight vector $w(n)$. The second term, $\mu \cdot u(n) \cdot e(n)$, on the right-hand side of Equation (3) represents the adjustment that is applied to the current estimate of the tap weight vector $w(n)$. The parameter μ is step size and the iterative procedure is started with an initial guess, $w(0)$.

In the control model, input data of the adaptive filter comes from the error output of the WFOV track loop as described in Figure 111. Number of taps is $M=20$ and step size parameter μ is determined empirically. Test results for the target motion input are shown in Figures 105-110.

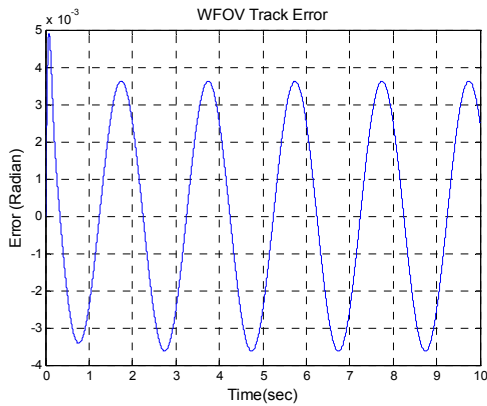


Figure 105. WFOV track error

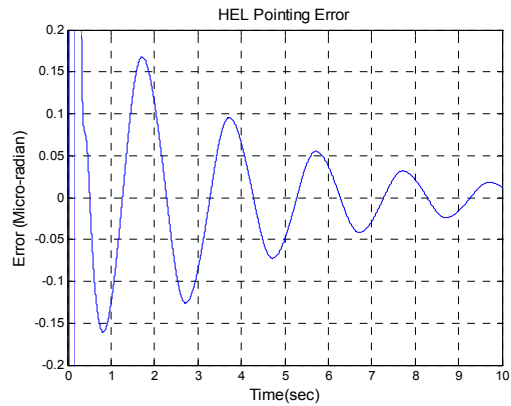


Figure 106. NFOV track error

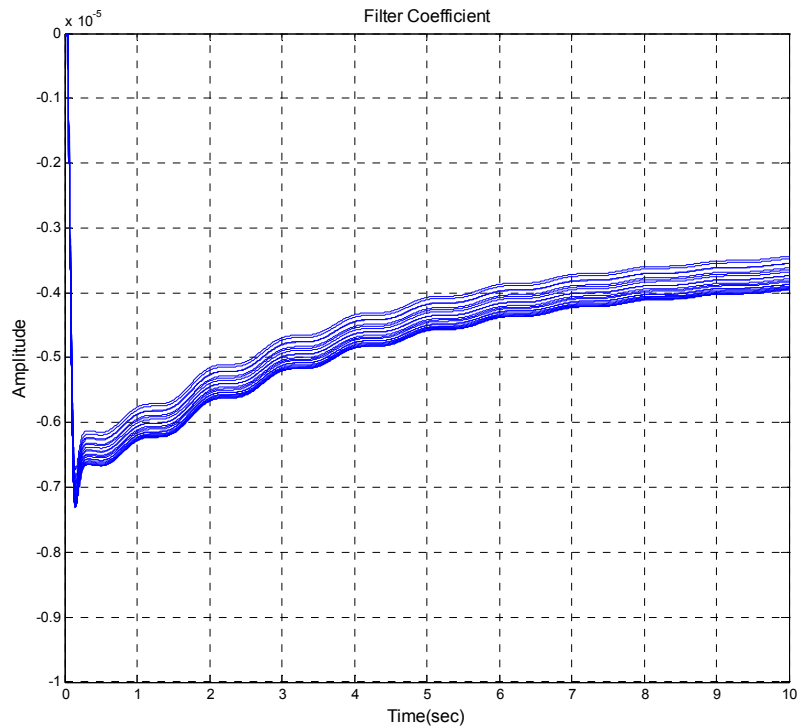


Figure 107. Convergence of filter coefficients

Figure 107 shows experimental plots of the convergence curves of the 21 tap weights for the step size parameter $\mu=2$. Initial values are 0 and all weights converge after 10 seconds. As the weights converge, tracking error of the NOFV loop is reduced as shown in Figure 106. When the step size parameter μ is increased, the rate of convergence of the LMS algorithm is correspondingly increased, i.e. the tracking error of the NFOV loop is quickly decreased as shown in Figure 108.

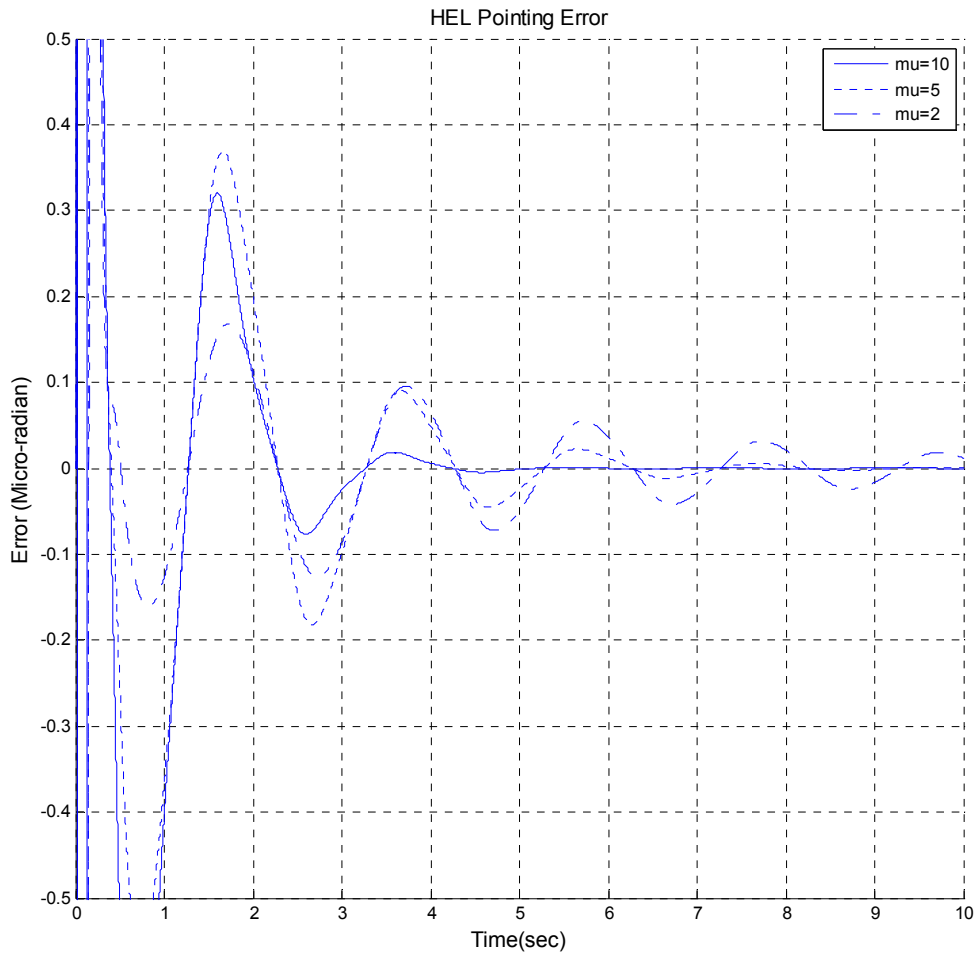


Figure 108. Learning curve of tracking errors for varying step size parameter

Figures 109-110 plot the error signals of the video tracking loop and show that error in the NFOV loop is not decreased as much as with compared to the F/F control

results. The reason is the adaptive LMS algorithm only decreases narrow band disturbance that is below the control bandwidth. In other words, Adaptive LMS is not effective for the rejection of the broad band disturbances.

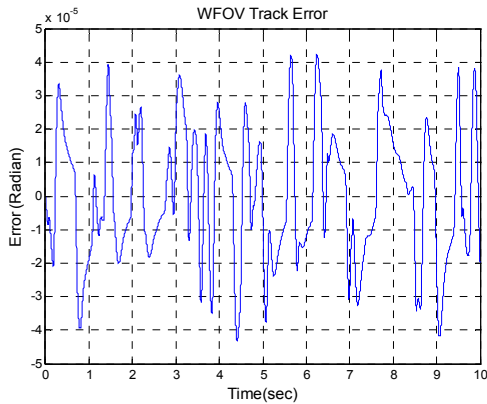


Figure 109. WFOV track error

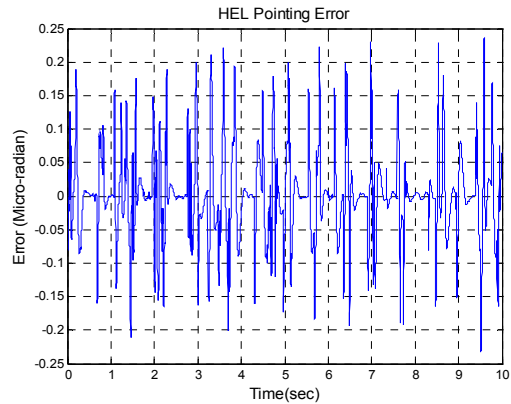


Figure 110. NFOV track error

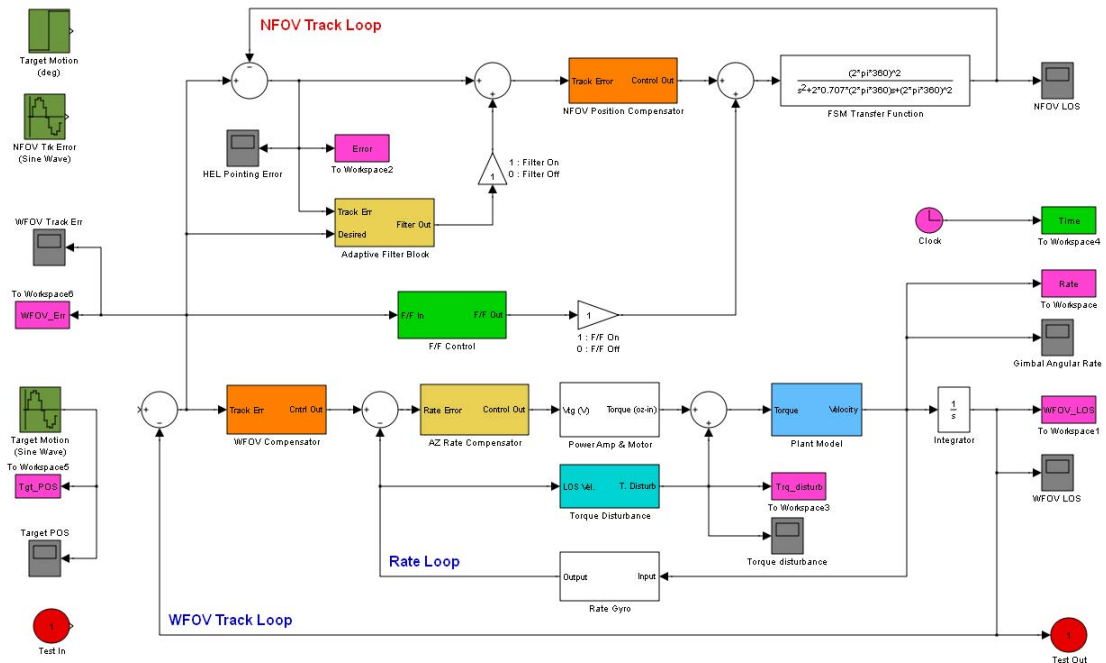


Figure 111. F/F control and adaptive filter

For the case of target motion along with external disturbance input, error of the NFOV loop is shown in Figure 112.

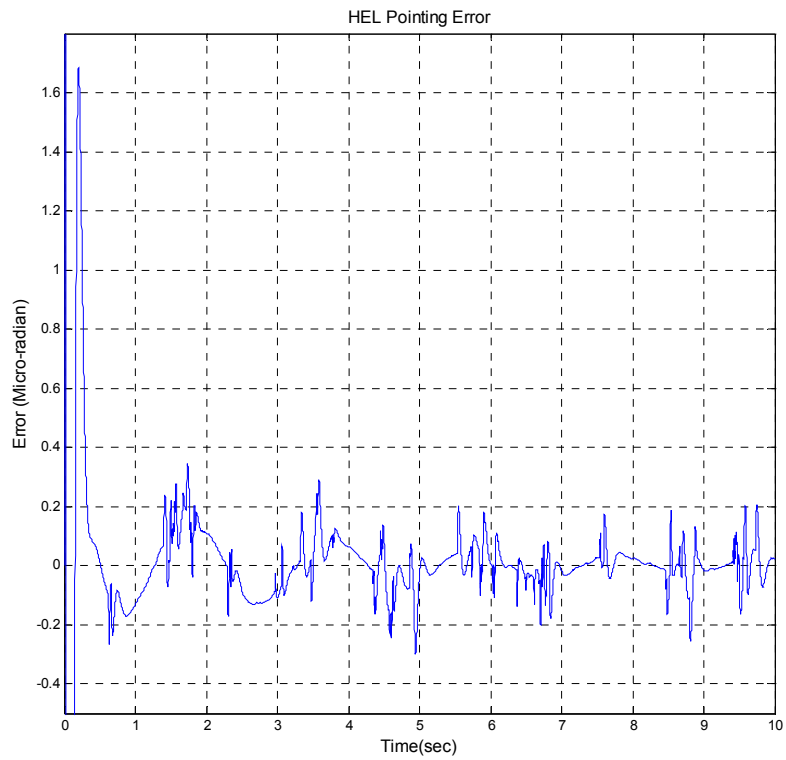


Figure 112. Error for target motion and disturbance

6. RESULTS AND CONCLUSION

System architecture of the HEL testbed including input/output interfaces and system operation modes and transitions are described. Based on the system configuration, some experiments on the WFOV and NFOV control loops were performed to investigate system characteristics and performance. A HEL system simulation model was also constructed based on the component model and experimental results to estimate system performance and to design new control algorithms for the improved performance. New control algorithms such as feed forward control and adaptive filters were applied to the system and it is shown that the algorithms improve the pointing performance as shown in Table 14. The results illustrate the effectiveness of adaptive feed forward control for a beam control system.

Table 14. Summary of system performance

	Classical controller	F/F controller	Adaptive filter with F/F controller
Track error	<80 mrad	< 0.3 mrad	< 0.02 mrad
Disturbance rejection	<10 mrad	< 0.025 mrad	< 0.02 mrad

A number of areas for future study. First is researching adaptive feed forward algorithms which manage broadband target motion and external disturbances. Secondly, control bandwidth of the WFOV and NFOV track loops need to be improved. Finally, developed algorithms should be implemented into the real testbed and subsequently verified. Although there may be still a little difference between the mathematical model and the real system, the control model is a good baseline to predict system performance when developing new algorithms. This report will be also helpful for basic understanding of the hardware and software of the HEL testbed.

THIS PAGE INTENTIONALLY LEFT BLANK

INITIAL DISTRIBUTION LIST

1. Defense Technical Information Center
Ft. Belvoir, Virginia
2. Dudley Knox Library
Naval Postgraduate School
Monterey, California
3. Prof. Jae Jun Kim
Department of Mechanical and Astronautical Engineering
Monterey, CA
4. Prof. Brij Agrawal
Department of Mechanical and Astronautical Engineering
Monterey, CA